Ocean Engineering 266 (2022) 112867

Contents lists available at ScienceDirect

Ocean Engineering

journal homepage: www.elsevier.com/locate/oceaneng

Real-time digital twin for ship operation in waves

Jae-Hoon Lee [a], Yoon-Seo Nam [a], Yonghwan Kim [a,*], Yuming Liu [b], Jaehak Lee [a], Heesuk Yang [a]

[a] Department of Naval Architecture and Ocean Engineering, Seoul National University, South Korea
[b] Department of Mechanical Engineering, Massachusetts Institute of Technology, USA

ARTICLE INFO

Keywords:
Digital twin
Ship operation in waves
Real-time prediction
Wave prediction
Seakeeping-maneuvering coupled simulation

ABSTRACT

This paper introduces a real-time digital twin for ship operations in seaways. The concept of the digital twin is becoming popular, and it is adopted for ship operation systems in this study. In particular, this paper introduces a new and innovative concept of the digital twin to predict ocean waves and hydrodynamic performances, such as seakeeping and maneuvering, which enables the risk and optimum route to be forecast in real time. An essential element in the realization of such a real-time digital twin is the real-time prediction of ocean waves. Hence, a sophisticated algorithm for wave reconstruction using measured wave-radar images is developed, which is extended to predicting the future evolution of a three-dimensional wave field in front of a ship within a time window of the order of 10 min. As another essential element, an analysis program to solve the coupled seakeeping-maneuvering problem is developed. This analysis can also be used in real time. By combining this with wave prediction software, the future occurrence of ocean waves and ship responses can be predicted. By extending this approach, the risk and performance of ships in various ocean environments can be predicted. In this paper, concepts, approaches, and examples are introduced.

1. Introduction

Marine engineers and operators envision operating a ship while predicting what will occur in the future. The mid-term and long-term voyage plans are generally determined based on daily weather forecasts in which a large-scale ocean wave field (spatial resolution of several kilometers) is predicted by statistical values such as significant height, mean period, and direction. On the other hand, in a short term, the current ship navigation involves visual observing the ocean waves that are currently occurring and operating while responding to them or determining the operating conditions based on the limited ocean information. However, if what a ship will experience in 10 or 20 min can be predicted according to the time evolutions of sea surfaces and tidal currents near the vessel by marine radar measurements in real time (Hilmer and Thornhill, 2015), ship operators will have many advantages, such as immediate decision-making on navigations to avoid any sudden risk or failure. This denotes the evolution of ship operation into a new concept in the short term.

As well known, the basic concept of a digital twin whose origin can be found in the aerospace industry consists of the physical asset in real space, the virtual model in cyberspace, and the connection of information between them (Grieves, 2014). Recently, digital twin technology has been adopted for integrated design & maintenance and performance & safety improvements for modern ship systems that are becoming increasingly complex. Giering and Dyck (2021) proposed a modular and feature-based Maritime Digital Twin Architecture (MDTA) based on a single source of information for all stakeholders over the whole lifecycle of a vessel. For the operational phase in this holistic vessel support, the concept of "DT aggregate", a platform for real-time integration, processing, and analysis of sensor data, and continuous exchange of information with physical assets through performance data and simulation results was introduced. In addition, Fonseca and Gaspar (2021) stated decision support that focuses on condition monitoring and simulation based on operation data as one of the main digital twin ship technology. For example, Bekker et al. (2018) established a plan to establish a real-time monitoring and decision-support system for a polar research vessel based on comprehensive measurements of ice load, hull vibration, shaft-line torque, and ocean environment, and Fonseca and Gaspar (2020) suggested the fundamentals of a digital twin (asset representation, behavior model, and measured data) for wave & ship motion monitoring and dynamic positioning. Regarding the advanced DT applications for ship operation, these studies emphasized real-time

* Corresponding author. Department of Naval Architecture and Ocean Engineering, Seoul National Univers ity, 1 Gwanak-ro, Gwanak-gu, Seoul, 08826, South Korea.
E-mail address: yhwankim@snu.ac.kr (Y. Kim).

https://doi.org/10.1016/j.oceaneng.2022.112867
Received 24 May 2022; Received in revised form 22 September 2022; Accepted 7 October 2022
Available online 18 October 2022

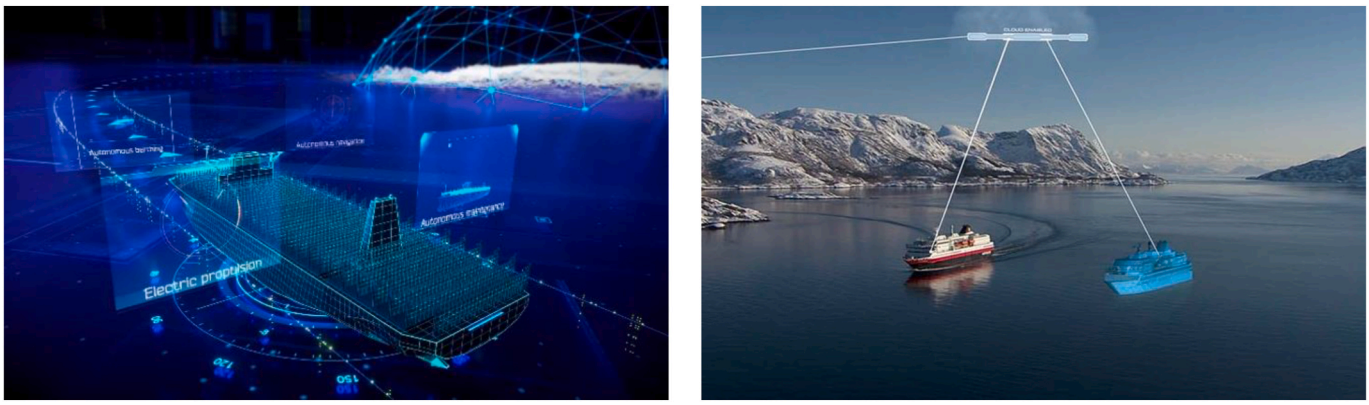

Fig. 1. Example concepts of digital ship of DSME (2021) and digital twin of DNV-GL (Smogeli, 2017).

virtual model realization and physics-based data analysis, simulation, and visualization for decision support based on physical environment measurements as well as physical asset performances. Fig. 1 shows examples of the concept of a digital twin for ship operations by DNV-GL (Smogeli, 2017) and the digital ship of Daewoo Shipbuilding and Marine Engineering (DSME, 2021).

Two main barriers hinder the application of the concept of digital twins to real-time ship operation. The first barrier is the technical difficulty in ocean environment prediction, particularly in the prediction of wave evolution at the locations in which a ship will pass in the near future. Current technology for wave prediction is mostly based on statistical analysis and relatively long-term predictions, e.g., in the order of days or weeks, which are predicted mostly by weather centers. The actual evolution of the wave profiles in space and time is required for the prediction of the actual motion responses/signals and potential risk. The second barrier is that all analyses and predictions must be performed in real time. In other words, the prediction of motion responses and maneuverability must be performed instantaneously without a time delay. Furthermore, if the ship operator, e.g., the captain, decides to change the operation conditions such as speed and heading, the resultant performance must be foreseen in a very short time.

In the present paper, the development of a real-time digital twin for ship operations is introduced. The primary service value is to predict seakeeping quantities such as wave-induced motions and loads and resulting operation performances of the ship in real sea states. Specifically, short-term deterministic predictions are performed based on sensor observations of marine radar images, ship motion records, and GPS data, and monitoring and forecasting results for target values are given via a dashboard to support ship operators' decision-making in real time. In accordance with the classification of digital services by Erikstad (2019), the system is an operational-level decision-support service for immediate ship navigations. In addition, it provides real-time insight into the current ocean environment and ship operations, and foresight information according to user-defined navigation scenarios; a future-cognitive system. A few new technologies have been developed and merged in the single system to overcome the two barriers mentioned above, and the simulation/computation time has been dramatically reduced.

Regarding ocean wave analysis, marine radar measurement technology has been developed to evaluate both statistical sea state parameters and spatiotemporal evolution of the sea surface (Neito-Borge et al., 1999a; Hessner et al., 2001). Currently, wave fields with a radius of 2–5 km can be measured through the X-band radar with sufficient resolution. Generally, three-dimensional (3D) fast Fourier transform (FFT)-based spectral analysis is applied to measured radar images to retrieve ocean wave information, but several important corrections and modifications are required for nonphysical spectral components induced by image shadowing and titling effects.

For wave-field reconstruction, Young and Rosenthal (1985) proposed linear dispersion relation-based filtering, and Nieto-Borge et al (2004) introduced a modulation transfer function (MTF) to attenuate nonphysical high-frequency components. Recently, Stole-Hentschel et al. (2018) introduced an enhanced MTF, considering the tilting effect more strictly. In addition, Zinchenko et al (2021a) suggested a modification method for the radar image itself that shifts the mean value such that the distribution of image intensity is similar to an actual wave field, and Qi et al. (2016) optimized numerical parameters for calibrations of image intensities and modifications of spectral components through comparison with higher-order spectral (HOS) method-based simulation results.

The reconstructed wave components were used to set the initial state of the wave field prediction. Wave propagation can be straightforwardly modeled using the dispersion relation of a linear gravity wave. Hence, adjustments for wave number and frequency are required for each discretized component obtained using FFT (Naaijen and Blondel-Couprie, 2012; Blondel-Couprie and Naaijen, 2012; Wijaya et al., 2015). Wave-field forecasting based on finite spatiotemporal measurement data is valid only for the predictable zone that is determined by the group velocities and propagation directions of wave components (Naaijen et al., 2014). Therefore, the predictability of the incident waves must be confirmed for specific time instants and locations by reflecting the characteristics of the ocean environment and ship operations (Qi et al., 2018). Recently, various nonlinear analysis techniques, such as an enhanced choppy wave model (Desmars et al., 2020), modified nonlinear Schrodinger equation (MNLS; Simanesew et al., 2017), and the HOS method (Wu, 2004; Kollisch et al., 2018; Fujimoto and Waseda, 2020) have been used to predict large-scale or severe ocean wave fields. Despite the better accuracy of nonlinear analyses, such models encounter large barriers for real-time analysis.

Various studies have been conducted on systems that predict the operational performance of a floating structure in actual sea states based on marine radar measurements. In the joint industry project, Onboard Wave and Motion Estimator (OWME), the ocean environment was evaluated using the FFT technique, and the phases of the discretized components were optimized for the predefined wave directionalities (Dannenberg et al., 2010). By combining the wave propagation model and pre-computed response amplitude operator (RAO) model, the incident waves and the resulting ship motions were forecasted (Naaijen et al., 2016, 2018). For the decision support system, Computer-Aided Ship Handling (CASH; Clauss et al., 2012), predictions were also performed on the wave-induced motion and hydrodynamic pressure distribution using a 3D FFT analysis. Recently, the HOS method was introduced to improve forecasting accuracy for severe ocean environments (Clauss et al., 2015). In addition, the Environmental and Ship Motion Forecasting system (ESMF; Alford et al., 2014; Kusters et al., 2016) applied a polar FFT or data assimilation procedure to a Doppler

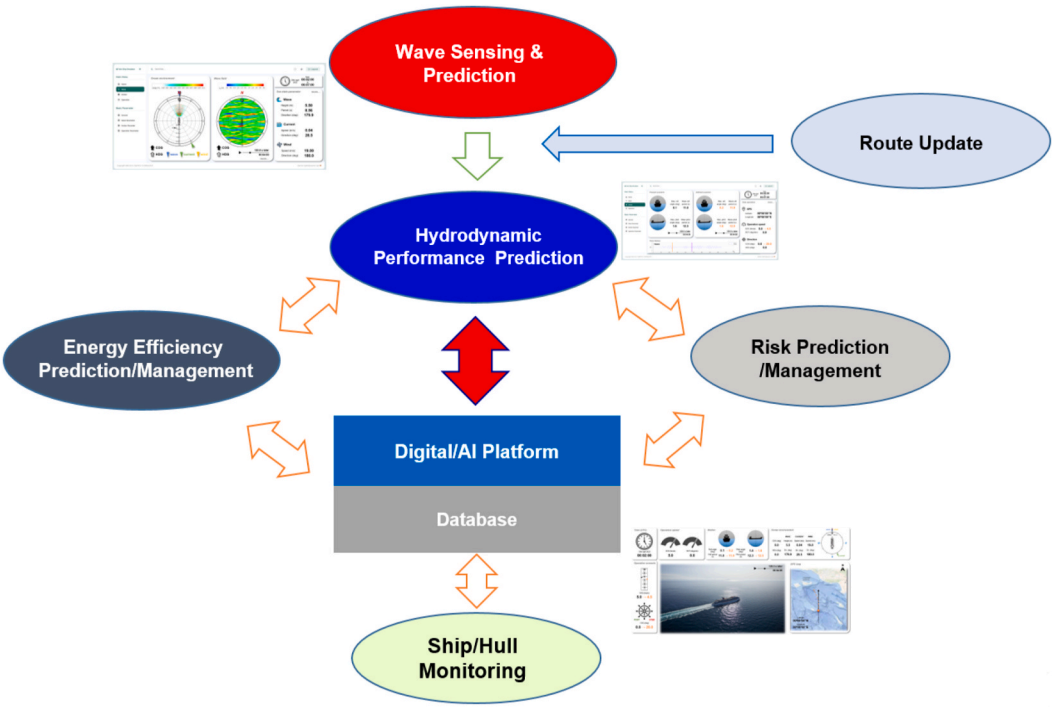

Fig. 2. Overall procedure of real-time digital twin.

radar signal (the orbital velocity of a wave particle) to reconstruct sea surfaces.

Various computational methods are available for seakeeping, and there is no need to describe the state of the art in this paper. However, methods applicable for real-time simulations are limited. In particular, seakeeping and maneuvering analyses must be coupled for ship navigation in the waves. In this study, an impulse response function (IRF) approach is adopted for the rapid simulation of ship motion responses and maneuvering in waves. The IRF method is popular for the seakeeping problem, but pre-computation is required for motion RAOs and IRFs. Furthermore, it must be extended to include the change in ship's speed and direction, i.e., encounter waves. In this study, a two-time scale model coupled with an IRF-based seakeeping and Maneuvering Modeling Group (MMG) for maneuvering (Lee et al., 2022) is integrated with a wave prediction model. The MMG model is the most popular method for maneuvering simulations.

The remainder of this paper is organized as follows. In Sec. 2, the basic concept and outline of the present digital twin system are explained, and the theoretical background for submodules are described: the reconstruction and prediction of ocean waves, the

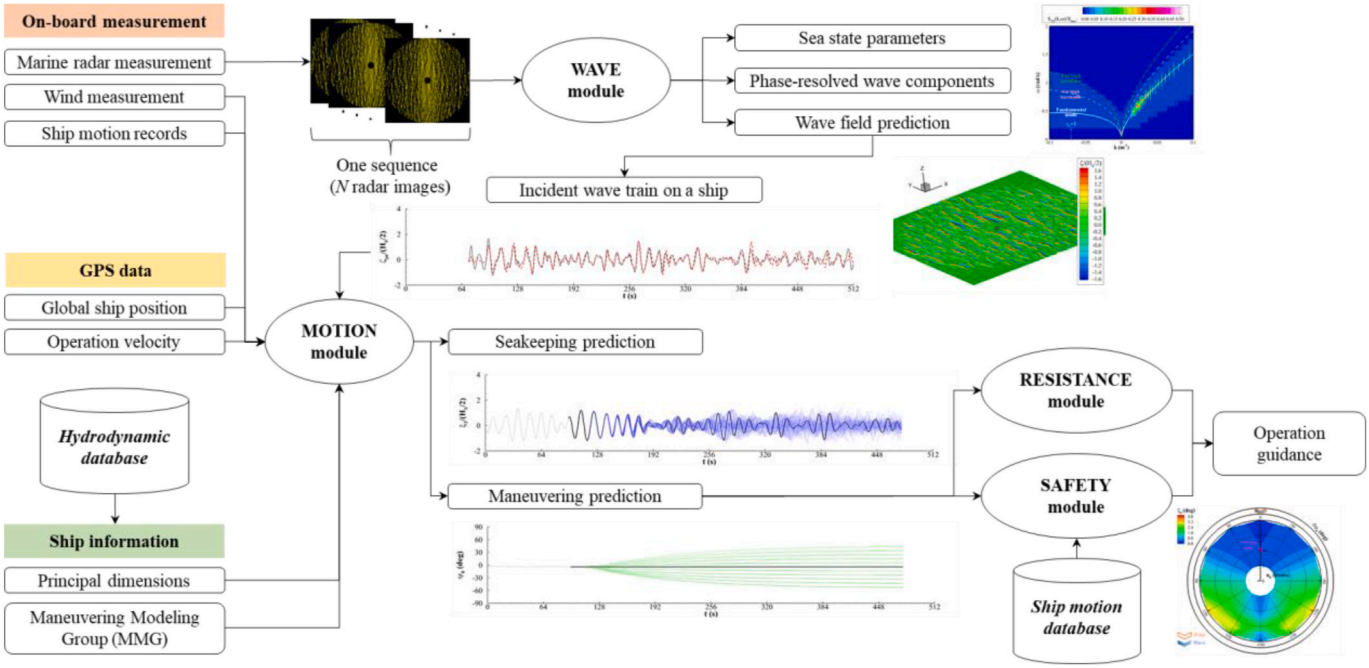

Fig. 3. Flowchart of overall real-time prediction system.

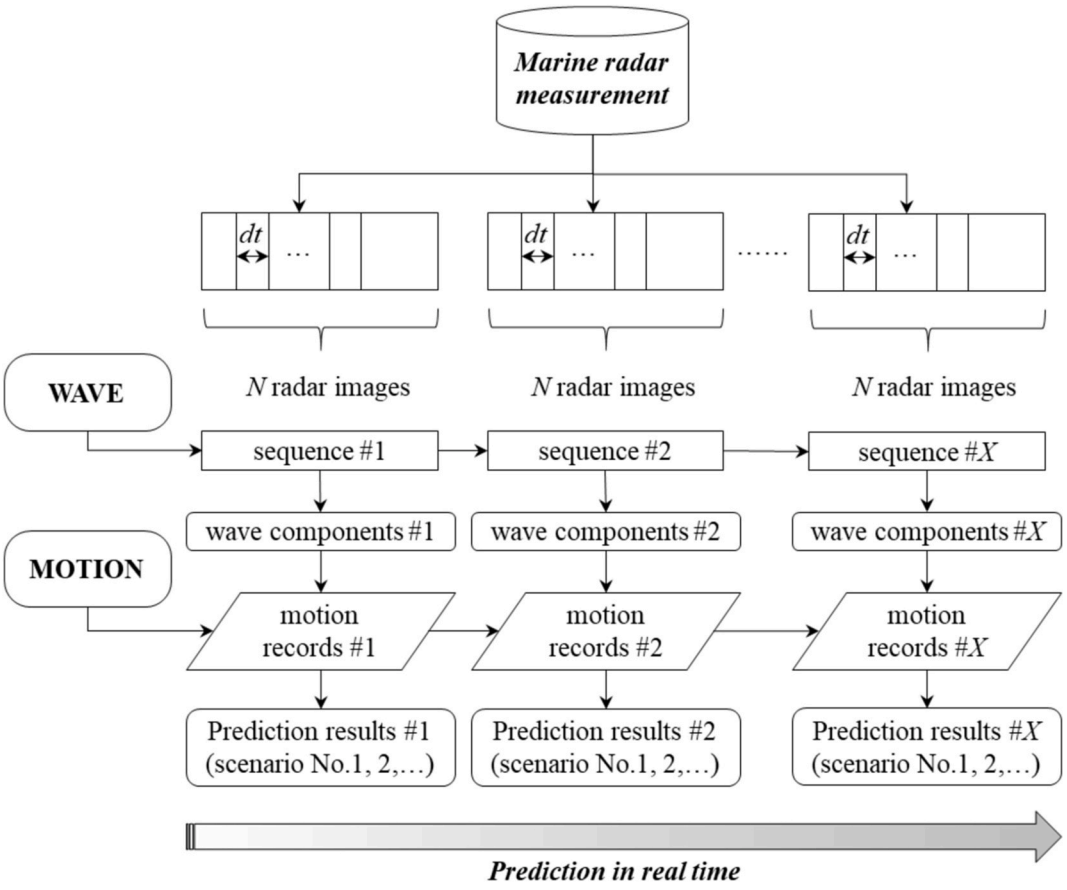

Fig. 4. Sequence-based simulation.

simulation of ship motion and maneuvering, and the operation guidance considering the resistance and seakeeping performance. The application examples validated by comparison with the numerical simulation data of the time-domain seakeeping-maneuvering coupling method (Lee and Kim, 2021) are presented in Sec. 3. This section includes the investigations of various technical issues regarding prediction performance such as the specifications of the radar image, filtering and modifications of the image intensity, and the considerations of ship operations relative to ocean environments. Finally, the conclusions are made in Sec. 4.

2. Real-time digital twin for ship operation

2.1. Basic concept

The digital twin for ship operations requires a few essential elements: wave prediction, analysis of the ship's hydrodynamic performance, and control platform for decision making and navigation control. These can be linked with and supported by various supplementary (but still important) functions such as risk prediction and avoidance, energy-saving operation, hull and equipment monitoring, and path optimization. A sample procedure of this integration is shown in Fig. 2.

To develop a digital twin, all analyses, simulations, predictions, and decision-making must be conducted in real time. The target time window in this study is of the order of 10 min. That is, the aim is to predict the wave evolution and ship responses within 20 or 30 min in the near future. This new digital twin system has the potential to support the operators' decision-making for the general navigation of a commercial ship. Deterministic identifications in minutes for specific wave trains and ship displacements (or accelerations) rather than statistical values for ocean environments can provide more concrete information to avoid any risks due to excessive ship operations. In addition, the predicted environmental loads (in particular, wave drift force and moment) can be utilized to determine the optimum course and speed. For now, the present digital service is not perfect in itself. In the future, parameterization of ship motions and wave loads to be reflected in ship navigations, and optimizations in terms of minimum response, resistance, and path distance should be added for a complete system.

2.2. System outline

The proposed real-time prediction system for ship operation consists of a "WAVE" module related to wave-field reconstruction and prediction, and a "MOTION" module related to simulating a ship's seakeeping and maneuvering performances. Additionally, "RESISTANCE" and "SAFETY" modules are also installed for the operation guidance. The flowchart is shown in Fig. 3.

The input data for the system are classified into three categories. The first is on-board measurement data, including marine radar images and wind measurements for the evaluation of the ocean environment near a ship. Moreover, wave-induced ship motions of all six degrees-of-freedom should be recorded for seakeeping computations by measurements through a typical onboard Motion Reference Unit (MRU). Second, GPS data such as the global position and operational velocity of a ship are necessary. Finally, in addition to the principal dimensions of a ship, a hydrodynamic database in the frequency domain (hydrodynamic coefficients, wave-induced excitation, and drift forces) and the Maneuvering Modeling Group (MMG; maneuvering derivatives, modeling for propulsion and steering) are required to simulate the ship operation.

Based on the input data, the WAVE module performs wave-field analysis to evaluate the sea state parameters (significant wave height, mean wave period and direction, and current information) and obtains

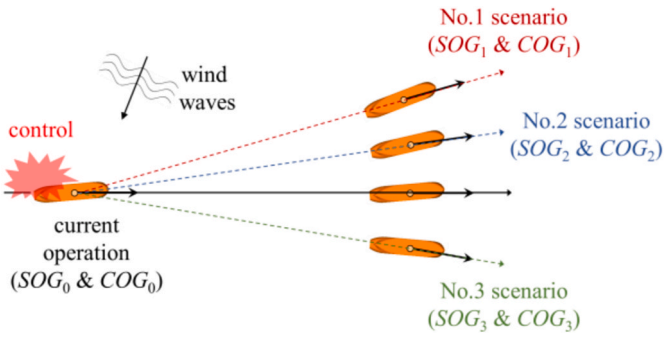

Fig. 5. Operation scenarios in prediction system.

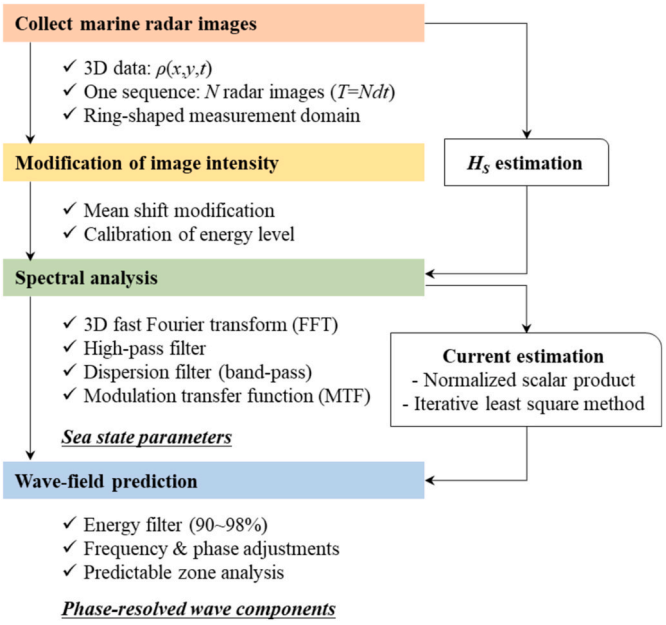

Fig. 6. Flowchart of WAVE module.

the phase-resolved wave components. According to the characteristics of the assessed ocean environments, the MOTION module conducts a deterministic seakeeping-maneuvering simulation in the time domain (for a certain predictable time range). Lastly, statistically or on average, the resistance performances and significant ship motions are evaluated in the RESISTANCE and SAFETY modules, respectively, and utilized to construct the operation guidance.

The system runs based on the sequence-based simulation as shown in Fig. 4. Analysis and forecast of the wave field are conducted for one sequence consisting of N radar images. For each sequence, the monitoring data (MRU and GPS data for current ship operation) is used as initial conditions for the seakeeping-maneuvering simulation. The results of a previous sequence are updated by that of a new sequence. Regarding future ship operations, the user can define an operation scenario by specifying the desired *SOG* (speed-over-ground) and *COG* (course-over-ground) as shown in Fig. 5. The operator-defined scenario is implemented by controlling the propeller revolution rate and rudder angle, which will be explained in detail in Sec. 2.4. The prediction results for various scenarios in a range set considering ship's maneuverability can be the database for decision support for optimum navigation. Actual ship navigations (monitoring data) and simulation results are linked via the operator's decision in real time. This denotes a continuous exchange of information between the physical asset and the virtual model.

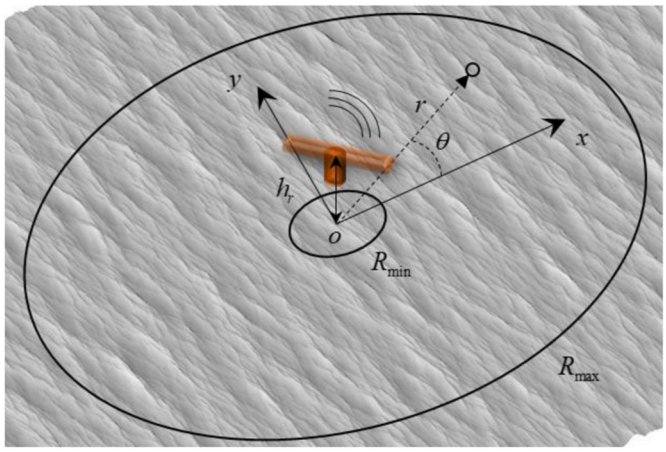

Fig. 7. Coordinate system and definitions in WAVE module.

2.3. Wave-field analysis

Fig. 6 shows the flowchart of the WAVE module. Computations in the module proceed largely to four steps: i) collection of radar images, ii) modification of image intensity, iii) spectral analysis, and iv) wave-field prediction. A detailed explanation of each step is as follows.

(1)Step 1: Collection of marine radar images

The marine radar measures the surrounding wave field (e.g., $\zeta_w(x,y,t)$) through the backscattered image intensity ($\rho_s(x,y,t)$) using the Bragg resonance phenomenon of sea clutter (Young and Rosenthal, 1985). The coordinate system and definitions are summarized in Fig. 7. Here, h_r is the installation height of the radar. The 3D spatiotemporal intensity data are constructed for a sequence of consecutive radar images, and the time interval (dt) between images is determined according to the radar rotation period (1.0–2.0 s). Furthermore, reliable measurements are possible only within a certain range, considering the specifications of the radar: minimum radius (R_{min}) of 200–500 m, and maximum radius (R_{max}) of 2–5 km. In this study, all the measurement data in a ring-shaped domain (Cartesian grid data) are utilized for the wave-field analysis.

(2)Step 2: Modification of image intensity

Radar images include physical ocean waves and nonphysical components owing to radar imaging mechanisms, such as shadowing and tilting effects. Therefore, prior to performing spectral analysis, modifications to the image intensity are required such that its distribution is similar to that of an ocean wave field. First, the mean-shift modification proposed by Zinchenko et al. (2021a) is applied. Generally, the image intensity has a value in 8-bit grayscale (0–255). Because the intensity has a positive mean value and is close to zero in the shadowing region, the distribution is significantly distorted compared with the actual wave elevations. Therefore, the mean value is corrected using the following equation.

$$\rho_m(x,y,t) = \begin{cases} \rho_s - \beta_m \rho_{mean} & \text{for non-shadowing} \\ 0 & \text{for shadowing} \end{cases} \quad (1)$$

where $\rho_{mean} = mean[\rho_s(x,y,t)]$ for non-shadowing.

Limited to the non-shadowing region, the intensity is shifted by the mean value multiplied by a factor (β_m). Generally, because more measurements can be performed for wave crests than for wave troughs, β_m has a value less than 1 (0.8–0.9). Moreover, the energy level of the image intensity is not uniform in space, unlike in an actual ocean wave field. Therefore, the following modification is performed to calibrate the energy level in the entire measurement domain:

$$\rho_c(r,\theta,t) = \rho_m(r,\theta,t) \Big/ \sqrt{\alpha_c(\theta)(r/R_{\max})^{\beta_c(\theta)}} \quad \text{where } \mathrm{var}(\rho_m(r,\theta,t)) \approx \alpha_c(\theta)\left(\frac{r}{R_{\max}}\right)^{\beta_c(\theta)} \tag{2}$$

where α_c and β_c are coefficients for approximating the variance distribution and can be obtained by applying the least square method to the measured data of a specific azimuth angle.

(3) Step 3: Spectral analysis

A 3D FFT-based spectral analysis (Nieto-Borge et al., 2004) is conducted to retrieve the sea state parameters and phase-resolved wave components from the radar images. The spatiotemporal image intensity can be expressed using spectral components, such that:

$$\rho(x,y,t) = \sum_{j=-\frac{J}{2}+1,m=-\frac{M}{2}+1,n=0}^{\frac{J}{2},\frac{M}{2},\frac{N}{2}} A_{jmn}\exp\left[i\left(k_{x,j}x + k_{y,m}y - \omega_n t + \varepsilon_{jmn}\right)\right]$$
$$\text{where } dk_x = 2\pi/L_x\, k_{x,j} = jdk_x, dk_y = 2\pi/L_y, k_{y,m} = mdk_y, d\omega = 2\pi/T, \omega_n = nd\omega. \tag{3}$$

Here, L_x and L_y indicate the image sizes in x- and y-directions, respectively. In addition, J and M are the numbers of data in each direction. The propagation direction of each discretized component can be determined according to the relationship between the signs of the total wave number ($k = \pm\sqrt{k_x^2 + k_y^2}$) and the wave frequency (ω).

Excessively low-frequency components due to the long-range dependent modulation effects in radar images are eliminated using a high-pass filter ($\omega_n < \kappa_1 d\omega$). The filtering range ($\kappa_1$) should be determined considering the spectral energy distribution of ocean waves (sea states and ship operations) and the minimum frequency ($d\omega$). In addition, another non-physical component in the image intensity, the shadowing-induced high harmonic component, is removed by a band-pass filter based on the linear dispersion relation. In other words, only the components for $\omega_n \in [\omega_0 \pm \kappa_2 d\omega]$ are taken into account, where ω_0 is the wave frequency corresponding to the total wave number for a deep sea ($\omega_0^2 = gk$) and κ_2 is the range of the dispersion filter. Lastly, the following MTF is applied to attenuate overestimated high-frequency components that cannot be removed by the filters:

$$A_{jmn}^{(MTF)} = A_{jmn}\left|M\left(k_{jm}\right)\right| \quad \text{where } M(k)^2 = \alpha_{MTF} k_{jm}^{-\beta_{MTF}}. \tag{4}$$

Here, α_{MTF} is the scaling coefficient according to the total energy of the wave field, and β_{MTF} represents the degree to which the high-frequency components are mitigated. The exponent of the MTF can be determined empirically using the known wave spectrum obtained by an independent measurement (e.g., a wave buoy). The wave field ($\zeta_{re}(x,y,t)$) can be reconstructed using the inverse fast Fourier transform (IFFT) for the modified spectral components.

(4) Step 4: Wave-field prediction

Based on the reconstructed components, the wave propagation model is constructed as follows. First, components with negligible en-

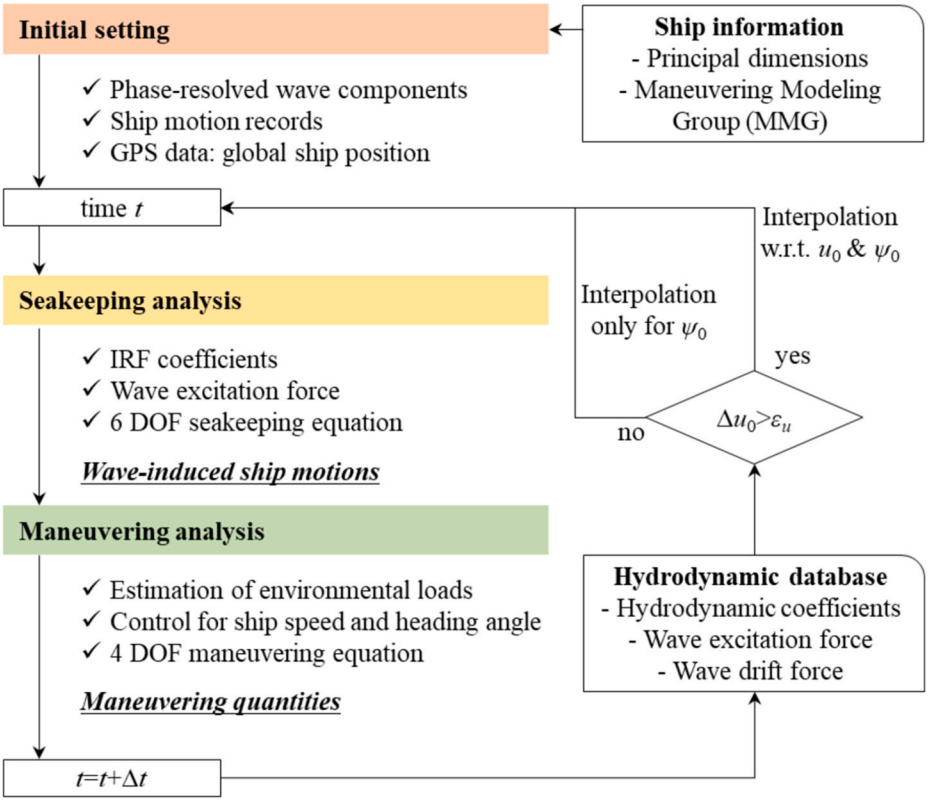

Fig. 8. Flowchart of the MOTION module.

ergy are removed for an efficient ship operation simulation (energy filter; the energy sum of the remaining components is 90%–98%). Subsequently, the frequency of each component is adjusted to satisfy the linear dispersion relation as follows:

$$\zeta_{pr}(x,y,t) = \sum A_{jmn} \exp\left[i\left(k_{x,j}x + k_{y,m}y - \omega_0(t-t*) + \varepsilon_{jmn} - \omega_n t*\right)\right]. \quad (5)$$

Here, $t* \in [t_0, t_0+T]$ is the reference time for the wave-field prediction. In other words, the waves propagate from the reconstructed field at $t = t*$. Hence, the phase of each component is adjusted such that $\varepsilon_{jmn} \rightarrow \varepsilon_{jmn} + (\omega_0 - \omega_n)t*$.

For a specific time and location, the predictability of each wave component depends on its group velocity ($c_g = \frac{\omega}{2k}\left(1 + \frac{2kh}{\sinh(2kh)}\right)$) and propagation direction ($\chi = \tan^{-1}(k_y/k_x)$). In other words, the component can be forecasted when the wave propagates from the measurement domain. The prediction index (PI) can be defined as follows.

$$PI(x,y,t) = \frac{\sum S^{(p)}_{jmn} dk_x dk_y d\omega}{\sum S_{jmn} dk_x dk_y d\omega}$$

$$\text{where } S^{(p)}_{jmn} = \begin{cases} S_{jmn} & \text{when } (x_{jm}, y_{jm}) \in [R_{\min}, R_{\max}] \\ 0 & \text{else} \end{cases},$$

$$x_{jm} = x + (t* - t)\left(c_{g,jm}\cos\chi_{jm} + u_c\right), y_{jm} = y + (t* - t)\left(c_{g,jm}\sin\chi_{jm} + v_c\right). \quad (6)$$

Here, S is the power spectrum of the discretized component ($S_{jmn}dk_x dk_y d\omega = \frac{1}{2}A^2_{jmn}$). PI indicates the energy sum of the predicted components compared with the total energy. In this paper, the predictable time range ($t \in [t_s, t_e]$) is defined as an interval with PI of 0.8 or higher at the radar location (the position of a ship; $(x,y) = (0,0)$).

For wave-field reconstruction, an additional estimation of the significant wave height is required. The significant wave height representing the total wave energy ($H_S = 4\sqrt{m_0}$) is used to scale the wave components (α_{MTF} of the MTF). Various estimation methods have been suggested using only the radar images without an independent measurement, such as the signal-to-noise ratio (SNR)-based empirical formula (Nieto-Borge et al., 1999b), statistical characteristics of shadowing effects-based methods (Gangeskar, 2014; Wijaya and van Groesen, 2016), and machine learning techniques (Salcedo-Sanz et al., 2015; Chen and Huang, 2021). In the present study, the significant wave height is assumed to be obtained through an independent measurement or estimation technique.

Information on the ocean current is necessary for the dispersion filter in spectral analysis. Conversely, the current can be estimated according to the distribution of the spectral components. First, components of 1%–2% or more of the maximum value of spectral energy are extracted for efficient computation (the nonphysical low-frequency components are also filtered out). When the dispersion filter is applied to the extracted components, an initial guess for the current at which the largest energy is obtained can be determined using a direct search method (the nondimensional scalar product method; Serafino et al., 2010). Thereafter, from the initial guess, the final estimation is performed using the iterative least square method (Senet et al., 2001; Huang and Gill, 2012) where the loss function is defined through a geometric error between the frequencies of a certain component and the linear dispersion relation. The process of extracting the fitting data using the dispersion filter and conducting the least square method is repeated for a converged current. Note that if a ship operates, the estimated value is the current relative to the ship's operational velocity.

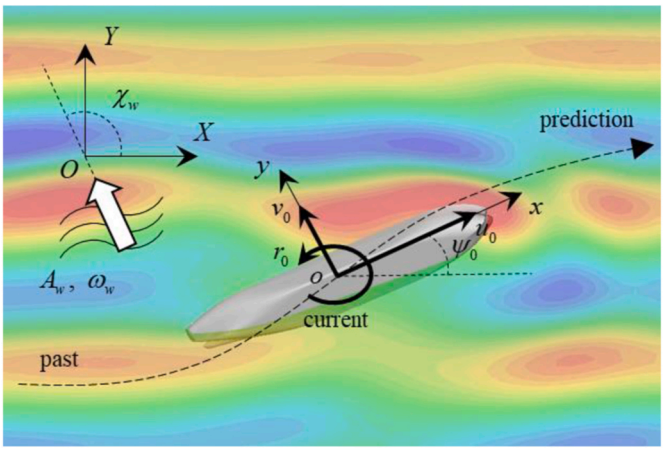

Fig. 9. Coordinate systems and definitions in MOTION module.

The demonstration case of short-term deterministic wave prediction based on X-band radar measurements through a similar procedure to the ocean wave field analysis in this study can be found in Zinchenko et al. (2021b).

2.4. Deterministic prediction for ship operation

For the forecasted incident wave trains on a ship, a two-time scale model-based seakeeping-maneuvering simulation is performed in the MOTION module (Lee et al., 2021). In the time-domain simulation, efficient computation should be performed based on the current state of ship operation. The overall procedure for the MOTION module is shown in Fig. 8. This procedure is briefly described as follows.

(1)Initial settings

As shown in Fig. 9, two types of reference coordinate systems are adopted in the module: global coordinate system (earth-fixed; $O-XYZ$) and inertial coordinate system (ship-fixed; $o-xyz$) translating with a ship's operational velocity (u_0: forward speed, v_0: sway speed, and r_0: yaw rotation speed). The yaw angle (ψ_0) of the ship is defined as the angle between the two coordinate systems. The transferred wave components from the WAVE module are redefined according to the coordinates such that:

$$\zeta_{pr}(x,y,t) = \sum_{w=1}^{N_w} A_w \exp\left[i\left(\begin{array}{l} k_w x\cos(\chi_w - \psi_0) + k_w y\sin(\chi_w - \psi_0) \\ +k_w(X - u_c T + X_T)\cos\chi_w + k_w(Y - v_c T + Y_T)\sin\chi_w - \omega_w t + \varepsilon_w \end{array}\right)\right]. \quad (7)$$

Here, N_w denotes the number of reconstructed wave components. Because the radar measurements are conducted with respect to the ship-fixed coordinate, the average trend of time-varying ship operation for the measurement duration ($t \in [t_0, t_0 + T]$) is reflected in the radar image. Therefore, the propagation direction of each component is corrected using the mean yaw angle such that $\chi_w = \tan^{-1}(k_{y,w}/k_{x,w}) + \psi_{mean}$. Furthermore, the phase is adjusted according to the ship position at the last instant of measurement by utilizing GPS data ($(X,Y)_{t=t_0+T} = (X_T, Y_T)$).

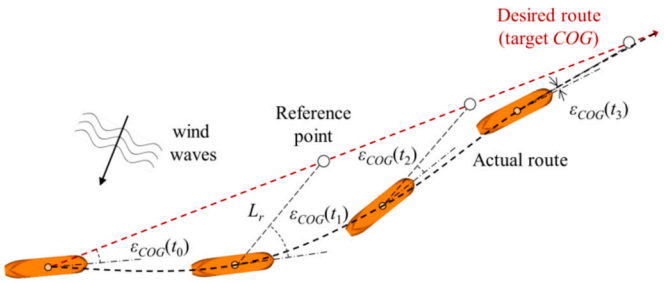

Fig. 10. Trajectory tracking method.

(2)Seakeeping analysis

The IRF method (Cummins, 1962) is used for seakeeping simulation. The six degrees-of-freedom (DOF) equations of wave-induced ship motions, ξ_i $(i = 1, \cdots, 6)$ can be expressed as

$$\left(M_{jk} + M_{jk}^{\infty}\right)\ddot{\xi}_k + \int_{-\infty}^{t} R_{jk}(t-\tau)\dot{\xi}_k(\tau)d\tau + \left(C_{jk} + C_{jk}^{R}\right)\xi_k = F_{ext,j}. \tag{8}$$

Here, M and M^{∞} indicate the mass matrix and the infinite-frequency added mass, respectively. C and C^R are the hydrostatic and radiation restoration coefficients, respectively. The memory effects of ship motion-induced radiated waves are considered by the retardation function $(R(t))$, which has the following relationships with the hydrodynamic coefficients, added mass $(A(\omega))$, and damping coefficient $(B(\omega))$:

$$\begin{aligned} R_{jk}(t) &= \frac{2}{\pi}\int_0^{\infty} B_{jk}(\omega)\cos(\omega t)d\omega \\ M_{jk}^{\infty} - \frac{C_{jk}^{R}}{\omega^2} &= A_{jk}(\omega) + \frac{1}{\omega}\int_0^{\infty} R_{jk}(\tau)\sin(\omega\tau)d\tau. \end{aligned} \tag{9}$$

To obtain the retardation function, a set of hydrodynamic coefficients for a wide range of frequencies, which depends on the operational velocity of the ship, is required. Moreover, the wave excitation forces for the discretized wave components (F_{ext}) can be evaluated based on the transfer functions of the amplitude and phase, which also depend on the ship's speed and heading angle $(\chi_w - \psi_0)$. For the real-time simulation, the retardation function and excitation force are computed considering the ship operation at a specific time through interpolation of the pre-computed hydrodynamic database. In this study, the frequency-domain database was constructed using the 2D strip theory (**Salvesen et al., 1970**). Since the 2D method has limitations regarding low-frequency wave radiations and forward-speed effects, more accurate seakeeping computations can be conducted by using the hydrodynamic coefficients obtained by model tests or advanced numerical methods such as the 3D panel method and CFD. For efficiency, the update of the dataset according to the operational velocity is performed only when the forward speed changes above a specific value $(\Delta u_0 > \varepsilon_u$; 0.1 to 0.2 knots), while interpolation with respect to the heading angle is implemented for every time step.

(3) Maneuvering analysis

Under the quasi-steady assumption that the characteristic time scales of the seakeeping and maneuvering motions are significantly different, the slowly varying maneuvering quantities are computed independently. The MMG-based 4-DOF maneuvering equation is defined as follows.

$$\begin{aligned} m(\dot{u}_0 - v_0 r_0) &= X_H + X_P + X_R + X_{wind} + X_{wave} \\ m(\dot{v}_0 + u_0 r_0) &= Y_H + Y_P + Y_R + Y_{wind} + Y_{wave} \\ I_{xx}\dot{p}_0 &= K_H + K_P + K_R + K_{wind} + K_{wave} \\ I_{zz}\dot{r}_0 &= N_H + N_P + N_R + N_{wind} + N_{wave}. \end{aligned} \tag{10}$$

Here, m, I_{xx}, and I_{zz} denote the ship mass and mass moment of inertia in x- and z-directions, respectively, X and Y are the external forces in the surge and sway directions, respectively, and K and N indicate the external moments in the roll and yaw directions, respectively. The subscripts H, P, R, *wind*, and *wave* denote the hydrodynamic forces induced by the hull, propulsion, rudder, wind, and waves, respectively. The MMG for external forces and moments can be established based on model tests or numerical computations (resistance and self-propulsion tests, propeller-open-water test, static drift and circular motion tests, rudder force tests, etc.). The details of this model in a calm sea are available in Yasukawa and Yoshimura (2015).

The wind loads are estimated based on the wind speed and direction relative to the ship. For a specific hull form, the wind load coefficients for various directions can be obtained from the wind tunnel test results or a regression formula (ISO, 2015). Moreover, the second-order drift force and moment are introduced as wave loads. Similar to the excitation force, the wave loads are evaluated through the interpolation of a pre-computed database considering the ship's operational velocity and heading angle at a certain time instant. In this study, a wave drift force database for various ship operations was constructed using the time-domain 3D Rankine panel method (Lee and Kim, 2020; Lee et al., 2021).

For future ship operations, an operational scenario should be prescribed. The target values for a certain scenario are SOG_{target} and COG_{target}. For SOG_{target} which corresponds to the ship's total speed $(U = \sqrt{u_0^2 + v_0^2})$, the control variable is the propeller revolution rate (n_P), and the error is defined by $\varepsilon_{SOG} = SOG - SOG_{\text{target}}$. On the other hand, for COG_{target} (the straight route along the desired course direction), the steering based on a rudder angle control (δ) is implemented for the vessel which may be subjected to environmental loads in various directions. In this study, the trajectory tracking method is applied for course-keeping. To define a course error (the difference between actual and given routes), a reference point is set on the desired route with a certain distance (L_r; about 3–5 times the ship length) from the ship as shown in Fig. 10. Then, the angle between the ship's centerline and a line from midship to the reference point is used as the course error (ε_{COG}). The proportional-integral-derivation (PID)-based control is implemented to obtain the required change in the propeller revolution rate and rudder angle for the computed errors, such that:

$$\begin{aligned} \Delta n_P(t) &= -\left(k_P^{(n_P)}\varepsilon_{SOG}(t) + \int k_I^{(n_P)}\varepsilon_{SOG}(t)dt + k_D^{(n_P)}\frac{d\varepsilon_{SOG}(t)}{dt}\right) \\ \Delta\delta(t) &= -\left(k_P^{(\delta)}\varepsilon_{COG}(t) + \int k_I^{(\delta)}\varepsilon_{COG}(t)dt + k_D^{(\delta)}\frac{d\varepsilon_{COG}(t)}{dt}\right) \end{aligned} \tag{11}$$

Here, k_P, k_I, and k_D are the control gains. Those control gains are determined based on a trial-and-error test or accumulated voyage data. Details of the course-keeping simulation based on the trajectory tracking method can be found in Lee and Kim (2021).

2.5. Operational guidance

Operational guidance can be provided based on the efficiency of the fuel consumption and risk assurance. In the RESISTANCE module, the calm-water resistance and wind- and wave-induced resistances are provided to estimate the fuel consumption. Risk prediction and avoidance can be determined using the SAFETY module. Any algorithm related to safety, such as parametric rolling, excessive motion, and dynamic stability, can be included in this module. In particular, specific seakeeping criteria can be defined by motion responses or vertical & lateral accelerations at a certain location (the ship's FP and bridge) as suggested by Stevens and Parsons (2002) and Pipchenko and Zhukov (2010). By utilizing the present hydrodynamics-based model, not only can the statistical values (such as the root-mean-square and significant values) be extracted through transfer functions (motion RAOs), but the

Table 1
Free-running simulation conditions.

Designation	Specifications
Ocean environmental condition	
Sea state	Beaufort scale 8
Wind velocity, V_{wind} [m/s]	19.0
Significant wave height, H_S [m]	5.5
Mean wave period, T_{mean} [s]	9.1
Main direction, χ_M [deg]	180.0 (head sea), 90.0 (beam sea), 0.0 (following sea)
Directional spreading, χ_s [deg]	60.0
Ship information	
Ship model	KVLCC2 tanker (SIMMAN, 2008)
Reference speed, V_{ref} [knots]	15.5 ($Fn = 0.142$)
MMG model	Yasukawa et al. (2015)

seakeeping quantities over a certain time range can also be deterministically predicted. Considering the type and class of a given ship model and its operation condition, the user can define the safety criteria, and operational guidance can be established depending on whether the criteria are met or not for a certain navigation scenario.

This operational guidance can be developed to include an autonomous decision function based on an artificial intelligence scheme. The short-term prediction modeling based on hydrodynamics, which has limitations in considering the nonlinearities of seakeeping and maneuvering quantities and the uncertainties in ship navigations, can be advanced by combining it with the data-driven modeling obtained using machine learning technologies. Hence, a large amount of data obtained from ship operations in actual voyages must be collected, and data-mining technology must be adopted. Eventually, operational guidance can be provided based on the hydrodynamic aspect and by considering all other factors related to ship operation. For example, wave-induced global structural responses, fatigue, and local extreme loads, such as slamming, can be important factors. As long as such factors can be predicted in real time, analysis algorithms can be included in the operational guidance modules.

3. Applications

3.1. Simulation conditions

3.1.1. Ship model and free-running test

To validate the developed real-time prediction system, virtual free-running of the well-known KVLCC2 tanker was simulated under the ocean environment corresponding to the Beaufort scale 8. Table 1 summarizes the details of the simulation conditions. The ITTC spectrum and $\cos^2$ directional spreading were adopted to generate short-crested irregular waves of 650 wave components with random phases. It was

Table 2
Synthetic radar image.

Designation	Specifications
Radar height, h_r [m]	40.0
Min. radius, R_{min} [m]	200
Max. radius, R_{max} [m]	2,560, 5,120, 10,240
Resolution	1024 × 1024
Space interval, dx & dy [m]	2.5, 5.0, 10.0
Number of radar images	32, 64, 96
Time interval, dt [s]	1.0

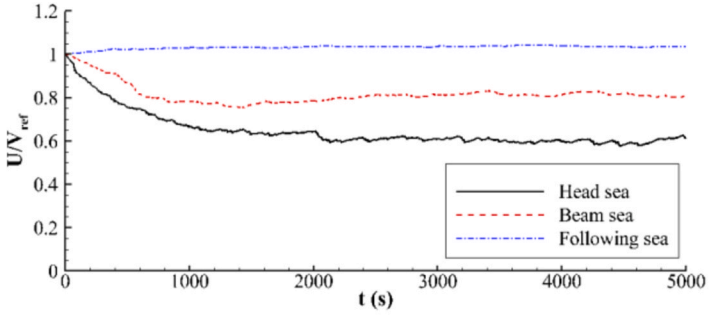

(a) Total speed, $U = \sqrt{u_0^2 + v_0^2}$

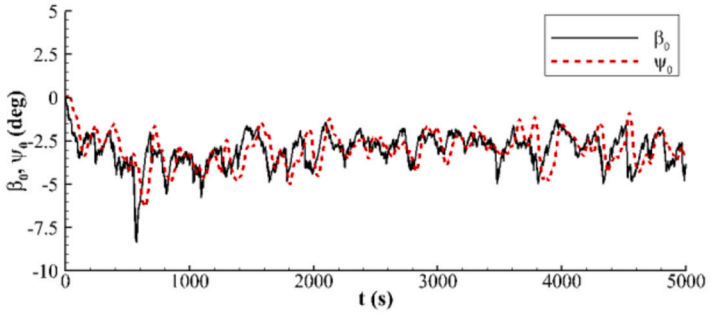

(b) Drift angle, $\beta_0 = \tan^{-1}(-v_0/u_0)$ and yaw angle, ψ_0 for beam sea condition

Fig. 11. Time histories of ship's operational velocity and yaw angle.

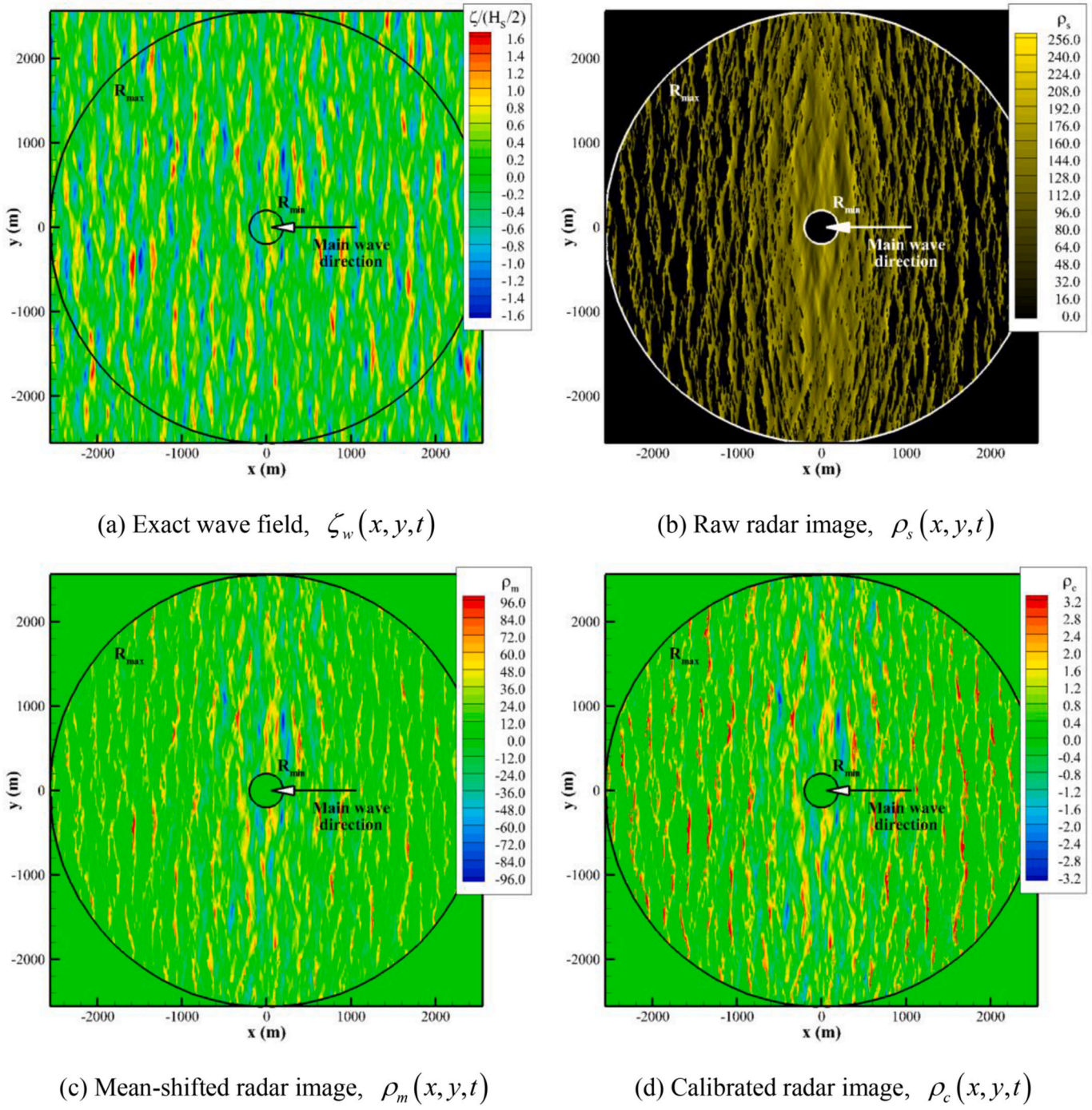

Fig. 12. Example of synthetic radar image: head sea condition, $T = 64\,s$, $R_{\max} = 2.56\,km$, $t = t_0 + T/2$

assumed that there was no ocean current.

Fig. 11 shows the time series of ship velocity and yaw angle. In free-running conditions, the ship navigated under a constant engine power that propels the vessel at the reference speed in calm water. The total speed was observed to reduce owing to the added resistance induced by the wind and waves. In particular, for environmental loads in the beam sea condition, steering was performed based on the trajectory tracking method to prevent the vessel from drifting, rotating, and maintain its route. Accordingly, the drift and yaw angles occurred to a similar degree such that the ship operated along a straight path.

3.1.2. Synthetic radar image

Using the free-running simulation results (global position and operational velocity of the ship), synthetic radar images were generated for the wave field around the ship. Considering existing marine radar technology, the specifications of the adopted radar image are summarized in Table 2. To investigate the prediction performance of the system, radar images of various sizes (different maximum sensing radii) were utilized with a constant resolution (1024 × 1024; the space interval is proportional to the image size). One image sequence consisted of 32, 64, or 96 radar images, and the time interval between the images was set to 1.0 s.

For a given wave field, the radar image was created by reflecting geometrical shadowing effects, which is one of the dominant imaging mechanisms at general grazing incidence. If the radar beam (the straight line between the radar receiver and the wave elevation at a measure-

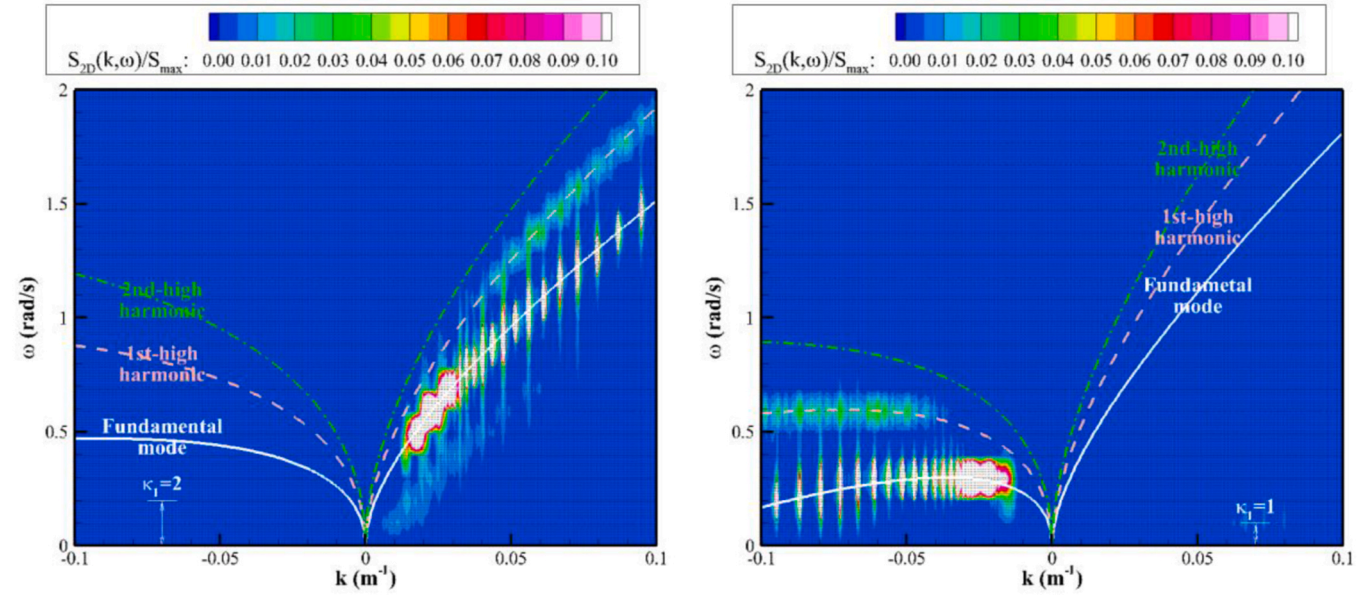

(a) Before spectral modifications

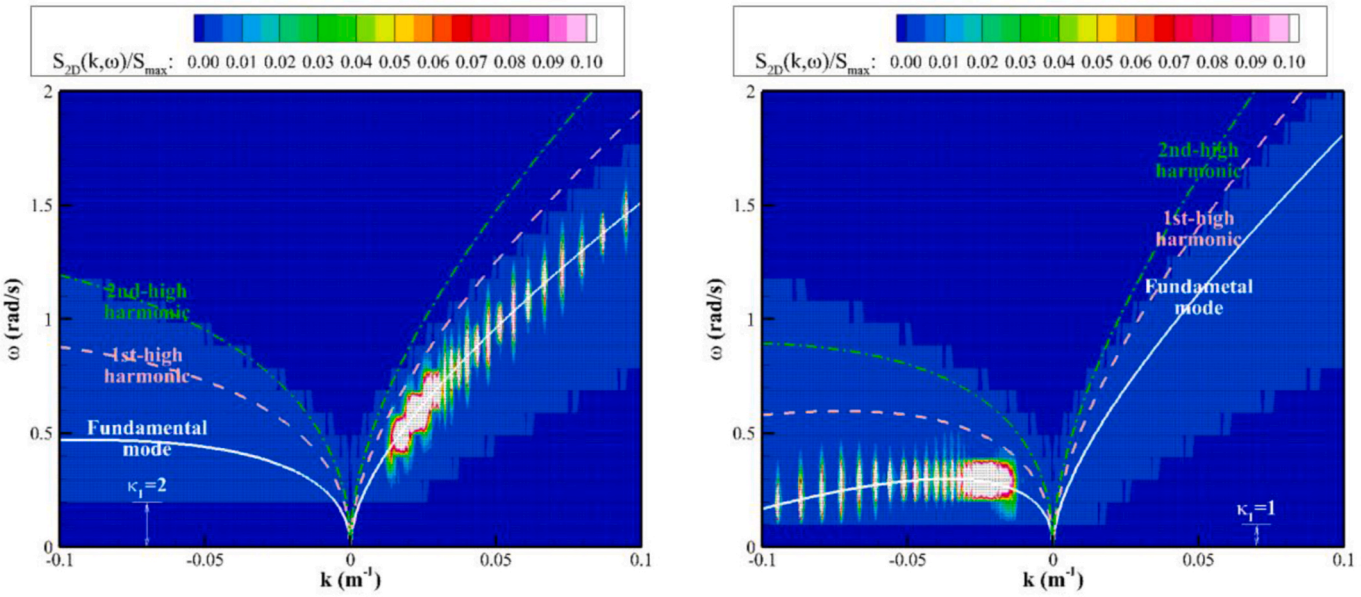

(b) After spectral modifications (filtering and MTF)

Fig. 13. 2D wave spectra, $S_{2D}(k,\omega)$: head sea (left) and following sea (right), $T = 64\,s$, $R_{\max} = 5.12\,km$

Table 3
Estimation for ship's operational velocity.

Ocean condition	Operational velocity, (u_0, v_0) [m/s]	
	Simulation	Estimation
Head sea	(5.27, −0.00773)	(5.24, −0.0141)
Beam sea	(6.21, 0.442)	(6.156, 0.482)
Following sea	(8.21, 0.00373)	(8.24, 0.0295)

ment location) is interfered with by the sea surfaces inside, the location is considered a shadowing region, where the image intensity is set to zero. On the other hand, for a non-shadowing region, the wave elevation is converted to an 8-bit grayscale (0–255), assuming that the intensity is proportional to the wave elevation. Fig. 12 shows an example of a synthetic radar image. The distribution of intensity differs significantly from the given wave field because of shadowing effects, and through the modifications for intensity, its distribution can have a wave-like form. It should be noted that the FFT-based spectral analysis was conducted for the Cartesian-grid rectangular domain containing a radar image. In other words, zero image intensity was assigned for the region outside the

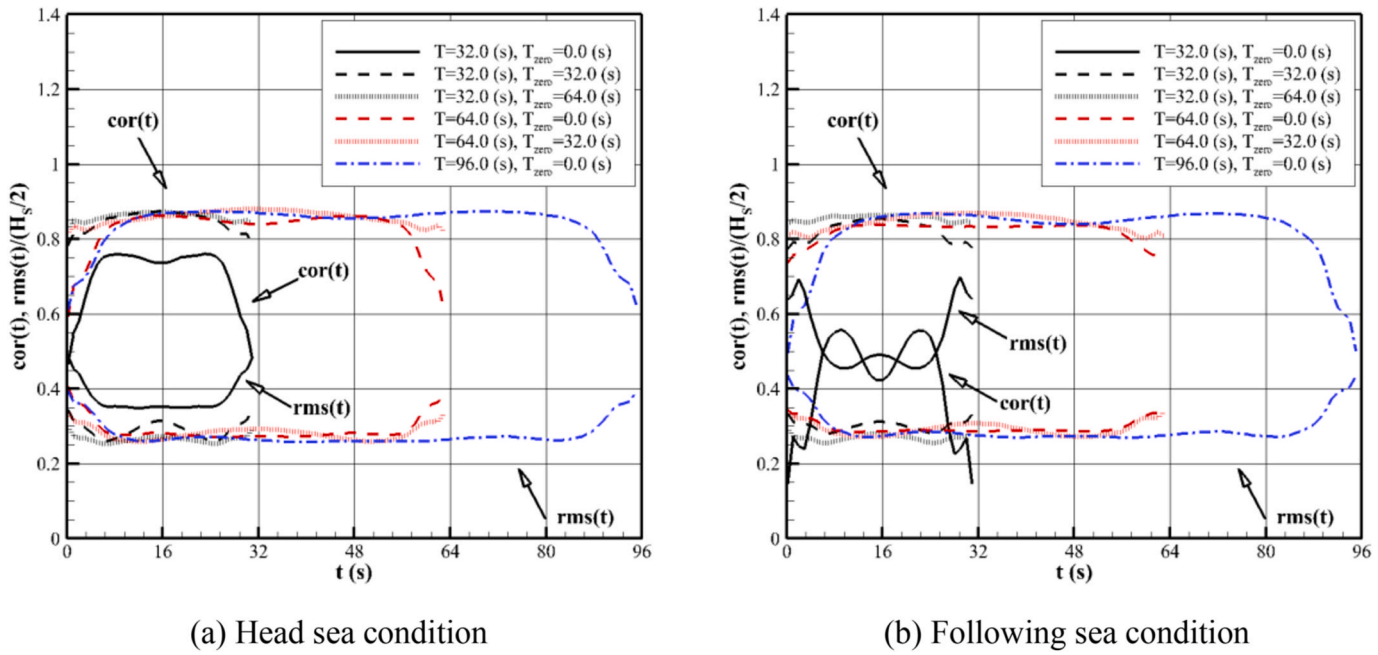

Fig. 14. Correlations of wave reconstruction results for different measurement durations: $R_{\max} = 5.12\,km$

measurement domain ($r < R_{\min}$ or $r > R_{\max}$).

3.2. Wave-field reconstruction

Fig. 13 shows the 2D wave spectra ($S_{2D}(k,\omega)$) normalized to their maximum value. A total of 64 radar images ($T = 64\,s$) with a maximum sensing radius of 5.12 km were used for spectral analysis. The starting instant of the image sequence was set as $t_0 = 1000\,s$ in the free-running simulation. The linear dispersion relation (fundamental mode) varied owing to the Doppler shift induced by ship operation.

It should be noted that the line of the fundamental mode in the figure was derived for the main wave propagation direction. As there was no ocean current, the ship velocity could be reversely computed using the current estimation technique ($(u_0, v_0) = -(u_c, v_c)$), as summarized in Table 3. As expected, based on the distribution of the spectral components, the slowly-varying operational velocity (maneuvering quantities; forward and sway speeds) could be estimated accurately compared to the mean value of the simulation data for the measurement duration. According to the shifted dispersion relation, nonphysical components were filtered out (the range of the dispersion filter: $\kappa_2 = 2$). The ocean-wave components of low frequencies were dominant in the following sea conditions compared with the head sea condition. Therefore, the range of the high-pass filter was set considering the wave propagation direction relative to ship operation (head sea: $\kappa_1 = 2$; following sea: $\kappa_1 = 1$) so that the low-frequency ocean-wave components which can induce restoring-dominant ship motions are not removed by the high-pass filter.

The wave-field reconstruction was validated by comparing it with the exact field used to create the synthetic radar image ($\zeta_w(x,y,t)$). To evaluate its accuracy, the following correlation ($cor(t)$) is defined:

$$cor(t) = \frac{\sum_{j=1}^{J}\sum_{m=1}^{M}\left(\zeta_{re}(x_j,y_m,t) - \mu_{re}(t)\right)\left(\zeta_w(x_j,y_m,t) - \mu_w(t)\right)}{\sqrt{\left(JM\sigma_{re}(t)^2\right)\left(JM\sigma_w(t)^2\right)}} \tag{12}$$

where $(x_j, y_m) \in [R_{\min}, R_{\max}]$ denotes the Cartesian-grid point in the measurement domain. In addition, μ and σ are the mean and standard deviation of the wave elevations, respectively.

Fig. 14 shows the reconstruction results for different measurement durations. Here, T_{zero} is the duration of zero-padding images. The duration of an image sequence is directly related to the resolution of the wave frequency ($d\omega$). Wave-field reconstruction was relatively inaccurate for the 32 images ($T = 32$ s) because of the coarse frequency resolution. This tendency intensified in the following sea conditions, where low-frequency waves were more dominant. For a longer image sequence, the correlation inside the domain was fairly high, according to the sufficiently resolved frequencies. In FFT analysis, which considers

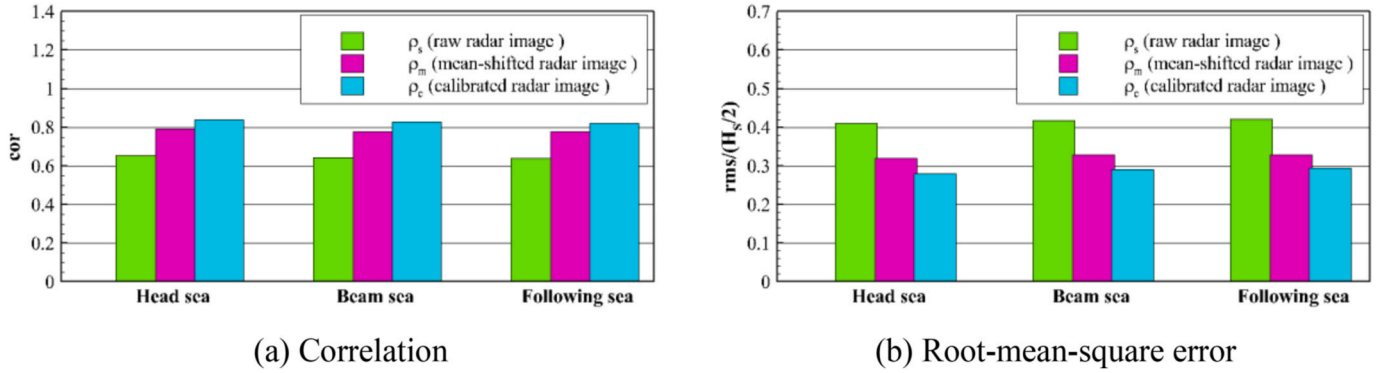

Fig. 15. Correlations of wave reconstruction results according to modifications of radar image intensity: $T = 96\,s$, $R_{\max} = 5.12\,km$

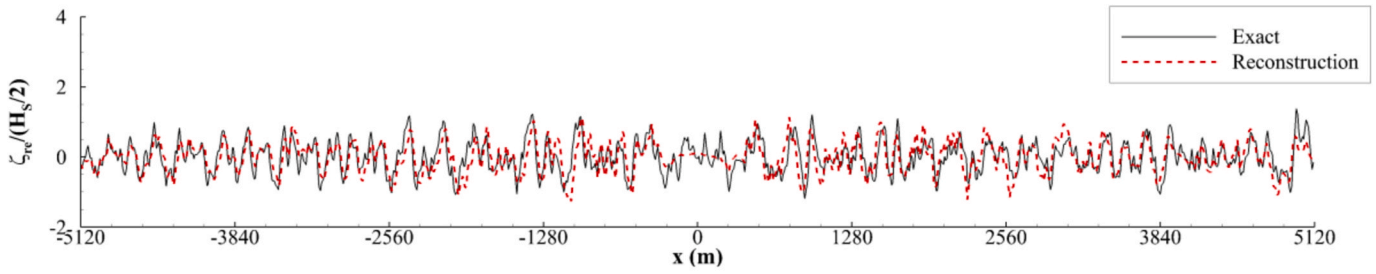

(a) Raw radar image, $\rho_s(x,y,t)$

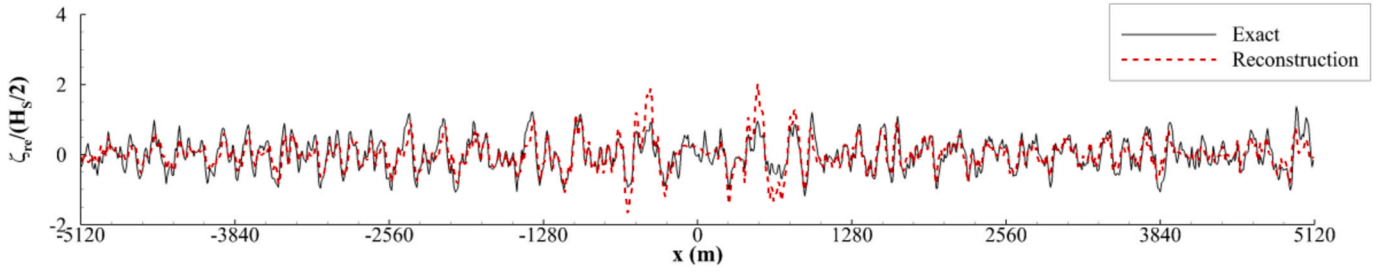

(b) Mean-shifted radar image, $\rho_m(x,y,t)$

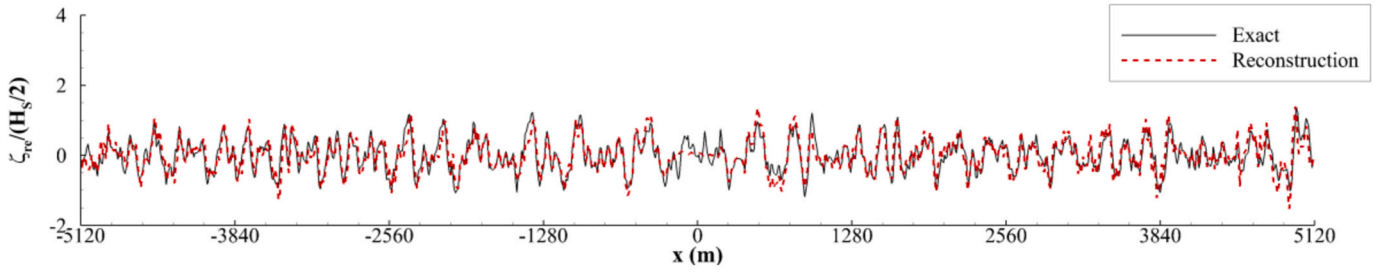

(c) Calibrated radar image, $\rho_c(x,y,t)$

Fig. 16. Reconstructed wave elevations: head sea, $T = 96\,s$, $R_{\max} = 5.12\,km$, $t = t_0 + T/2$, $y = 0$

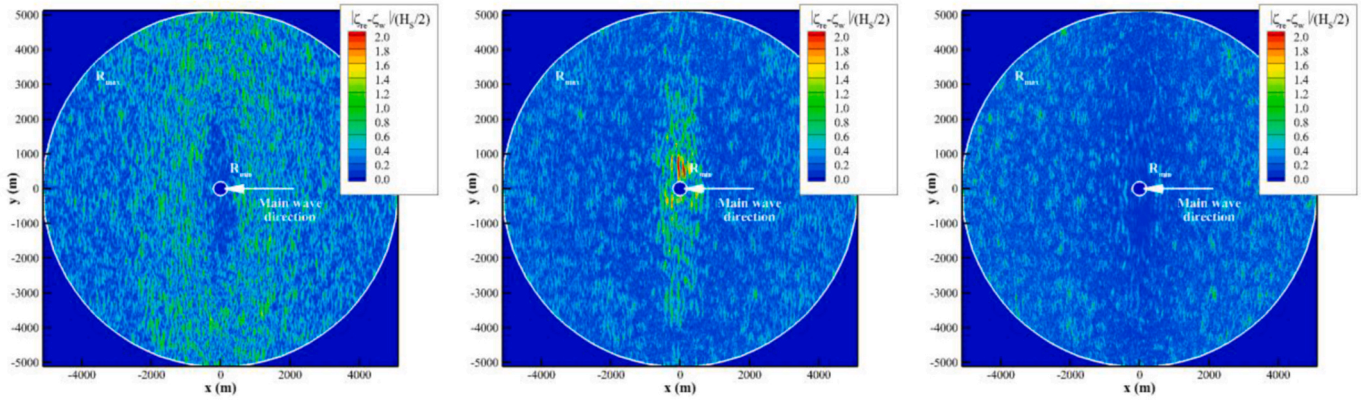

(a) Raw image, $\rho_s(x,y,t)$ (b) Mean-shifted image, $\rho_m(x,y,t)$ (c) Calibrated image, $\rho_c(x,y,t)$

Fig. 17. Error distribution of reconstructed waves: head sea, $T = 96\,s$, $R_{\max} = 5.12\ km$, $t = t_0 + T/2$

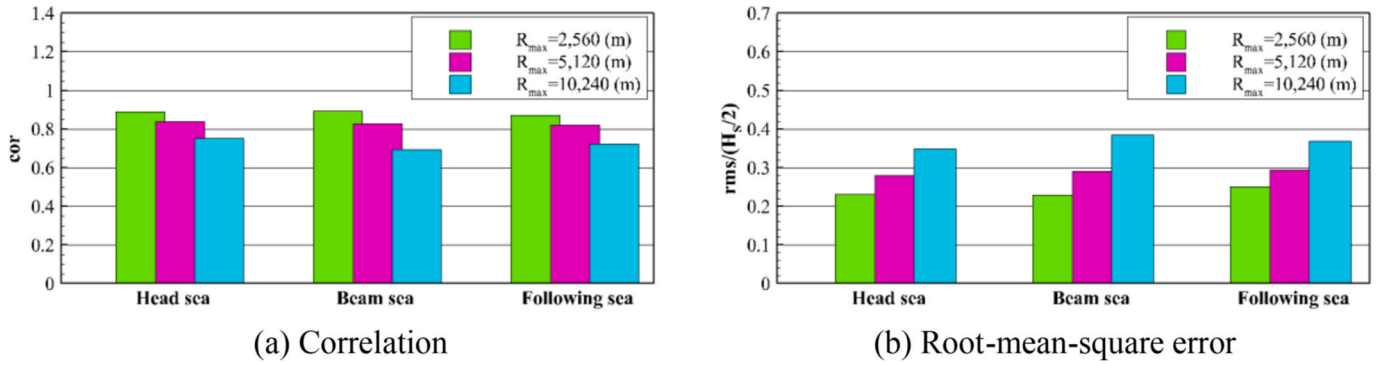

Fig. 18. Correlations of wave-field reconstruction results for different image sizes: $T = 96\,s$

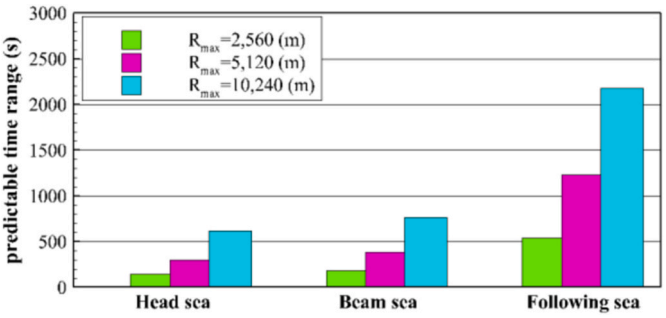

Fig. 19. Prediction time ranges for different image sizes: $T = 96\,s$

the data, periodic, nonphysical high-frequency components are generated owing to the discontinuity at a boundary (the Gibbs phenomenon). As such components were filtered out based on the linear dispersion relation, the correlation decreased at the boundaries. The root-mean-square (rms) errors between the exact and reconstructed fields showed similar trends to the correlation. By adopting zero-padding images, the errors at the boundaries were reduced and the reconstruction accuracy was improved through a finer frequency resolution. For both head and following sea conditions, it can be confirmed that a reliable wave-field reconstruction can be performed based on the frequency resolution corresponding to the measurement duration of $T = 64$ s or more (including zero-padding images).

The reconstruction results were compared according to the modifications in the image intensity (Fig. 15). For the raw radar image, the correlation was relatively low, at approximately 0.65. This was because its intensity contained high-frequency components induced by positive gray scaling, which was not physical, but satisfied the linear dispersion relation. Although the components were alleviated by the MTF, the reconstruction results differed from the exact wave field in terms of the amplitude and phase (Fig. 16(a) and Fig. 17(a)). For the wave-like form intensity distribution through mean-shift modification, the correlation, representing how much the phases of the two datasets coincide, increased remarkably to approximately 0.8. However, owing to the nonuniform energy level in the measurement domain, overestimations and underestimations for wave elevations were confirmed in the regions in which shadowing effects were severe and insignificant, respectively (Figs. 16(b) and Fig. 17(b)). These errors were mitigated by calibrating the energy level, and the correlation was improved to approximately 0.85 (Figs. 16(c) and Fig. 17(c)). The accuracy improvements by the calibration were greater for the rms errors (about 10%) because the overestimated wave elevations near the radar were alleviated. Overall, the reconstruction accuracy was slightly higher for head sea conditions according to the more scattered wave energies for a given frequency resolution.

The reconstruction results were compared for different image sizes

Table 4
Number of phase-resolved components.

Ocean condition	Maximum sensing radius, R_{max} [m]		
	2,560	5,120	10,240
Head sea	2,693	18,795	460,036
Beam sea	3,665	25,773	612,061
Following sea	2,760	20,614	489,280

Table 5
Computation time: Intel i7-4790/3.60 GHz CPU (single-core process).

Wave-field analysis	Duration of image sequence (T; s)			
	32.0	64.0	96.0	
	Computation time (s)			
	18.8	31.2	47.9	
Deterministic prediction (for 500-s simulation)	Number of wave components			
	2,000	5,000	10,000	20,000
	Computation time (s)			
	5.05	9.98	19.1	36.4

(Fig. 18). While the wave-number resolution (dk) increased for a larger maximum sensing radius, the resolution of the radar image was fixed at 1024 × 1024; therefore, the range of the discrete wave number (k_{max}) decreased because the space interval (dx and dy) was proportional to the radius. Accordingly, it was difficult to consider high-frequency wave components through a radar image of a larger domain, which resulted in a reduced correlation. Nevertheless, the correlation was confirmed to be 0.7 or higher for the 10.24 km-radius measurement. In conclusion, to accurately reconstruct the wave field, computation parameters such as the duration of an image sequence, specifications of a radar image, and filtering range should be optimized considering the ship operation.

3.3. Prediction of wave-field and ship motion

Using the phase-resolved wave components, deterministic predictions for wave trains incident on a ship and the resulting ship motions were conducted. Fig. 19 compares the predictable time ranges for different maximum sensing radii and ocean conditions. Under head sea conditions, the range was relatively short because the wave components passed rapidly through the ship. However, the range was significantly longer for the following sea conditions, where the waves propagated in the same direction as the ship operation. The range was observed to be almost proportional to the image size. Through the 5.12 km radius measurements, it was possible to forecast the incident waves for approximately 5 min in the head sea and approximately 20 min in the following sea. However, for a larger measurement domain, the number of reconstructed wave components increased significantly according to the finer wave number resolution, as summarized in Table 4 (when

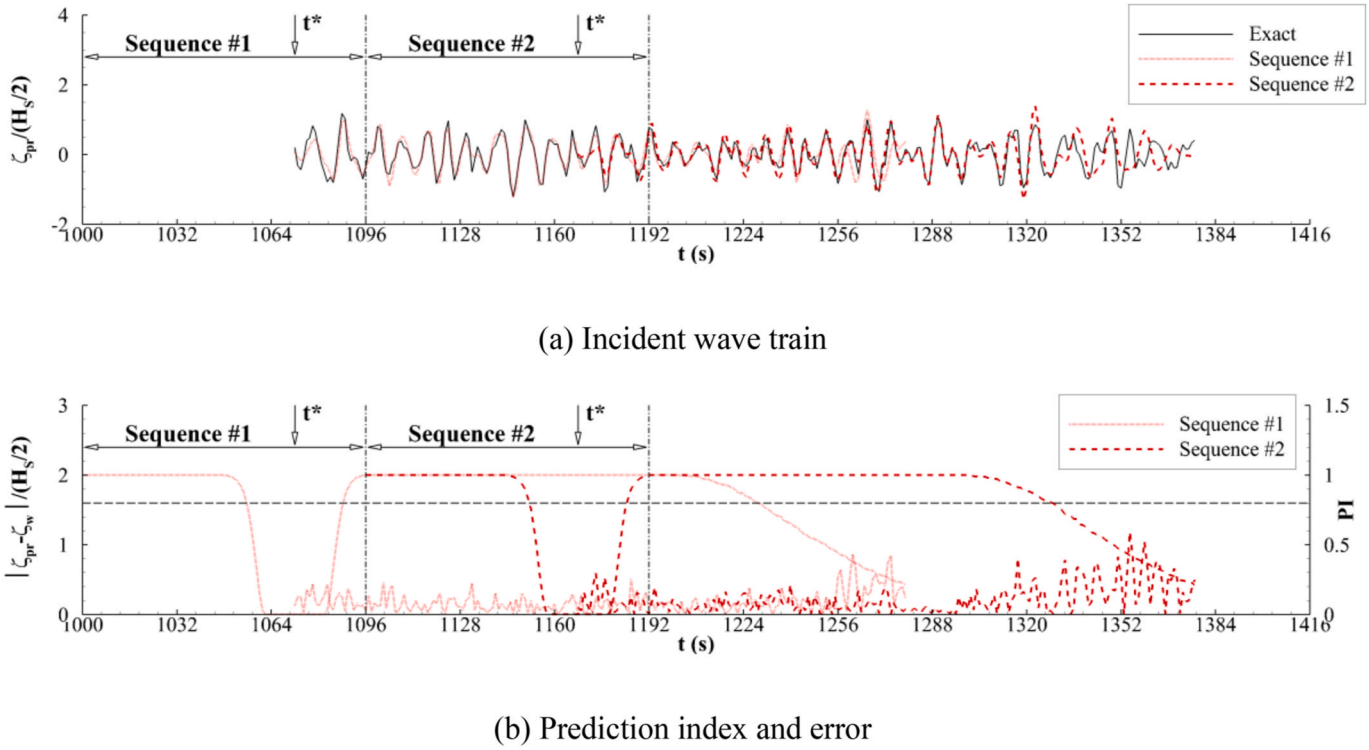

Fig. 20. Prediction for incident waves: head sea condition, $T = 96\,s$, $R_{\max} = 2.56\ km$

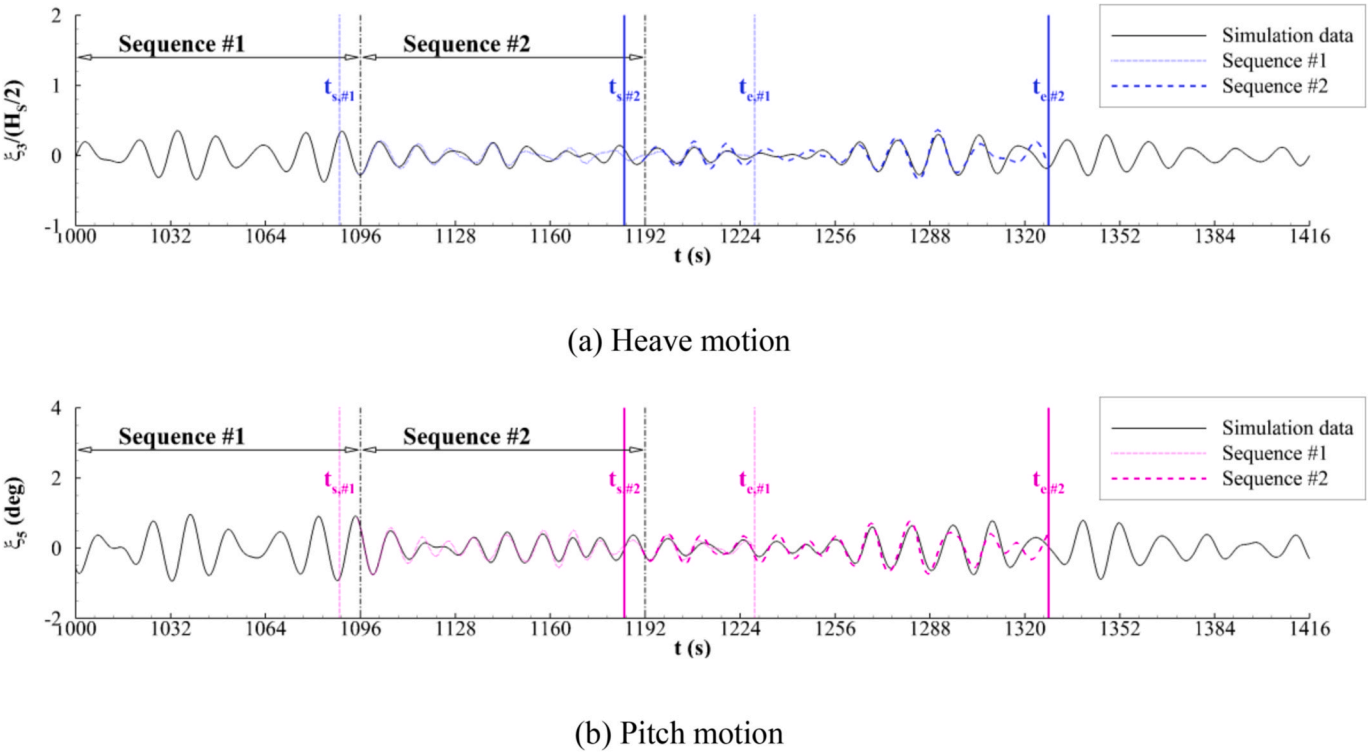

Fig. 21. Prediction for ship motions: head sea condition, $T = 96\,s$, $R_{\max} = 2.56\ km$

applying the 90% energy filter). An excessive number of components causes difficulties in the real-time simulation of ship operation owing to high computational costs; therefore, an appropriate setting for the sensing radius is required.

To operate the system in real time, the sum of the computation times for wave-field analysis and deterministic prediction should be shorter than the duration of an image sequence. Table 5 shows the CPU times for this analysis when a typical single-core process, Intel i7-4790/3.60 GHz CPU processor, was used. Approximately 48.0 s were required to extract the phase-resolved wave components from 96 radar images, i.e., 96-s

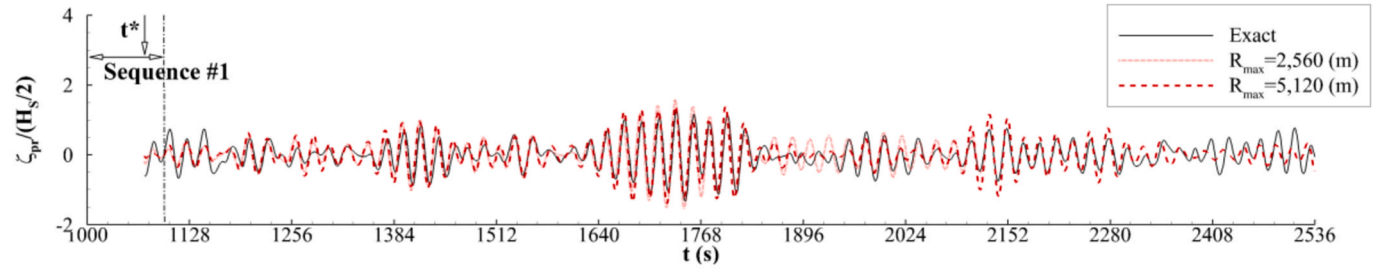

(a) Incident wave train

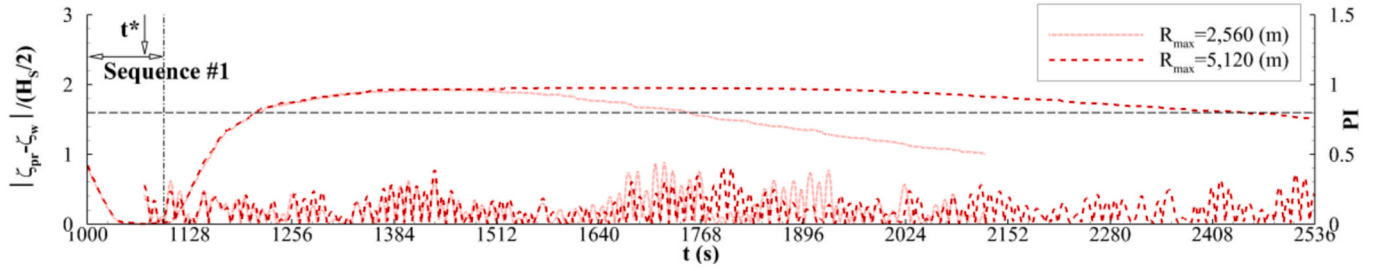

(b) Prediction index and error

Fig. 22. Prediction for incident waves: following sea condition, $T = 96\ s$

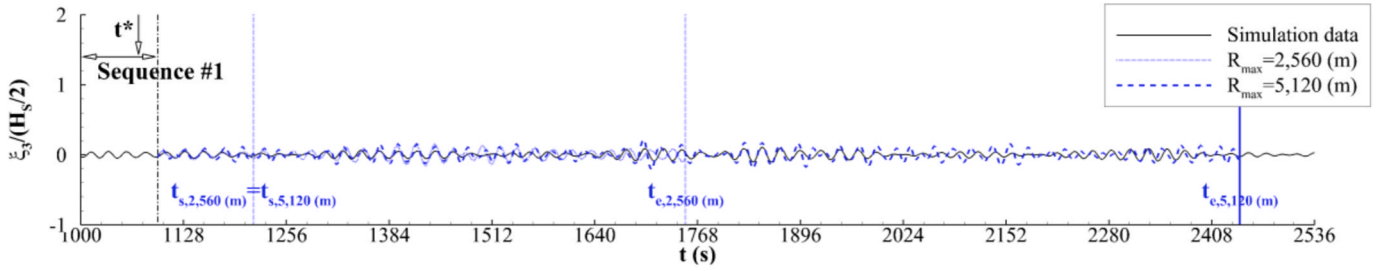

(a) Heave motion

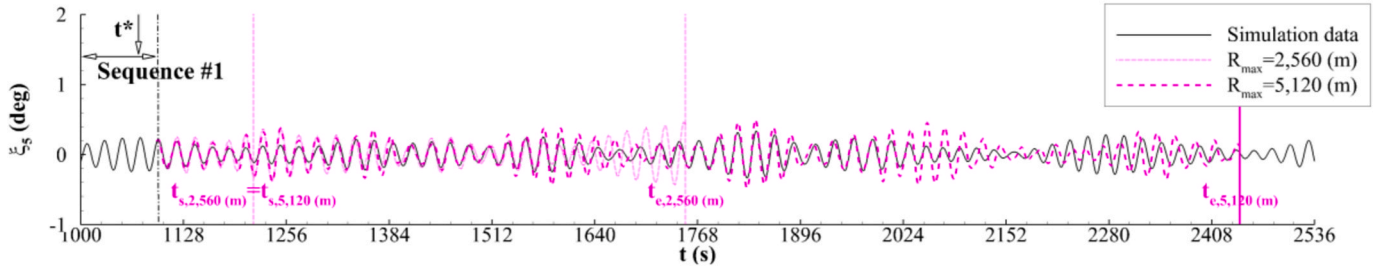

(b) Pitch motion

Fig. 23. Prediction for ship motions: following sea condition, $T = 96\ s$

time window. Furthermore, the prediction of waves and ship using 20,000 wave components required approximately 36.5 s for a 500-s simulation. Naturally, components that can cover a wider range of wave fields require more computational time. Therefore, an appropriate sensing radius setting is required. Alternatively, an additional data assimilation procedure should be performed to approximate the ocean wave field using a smaller number of components. Note that the computational time can be reduced significantly by using faster or multiple processors.

Fig. 20 shows the wave prediction results for the head sea conditions.

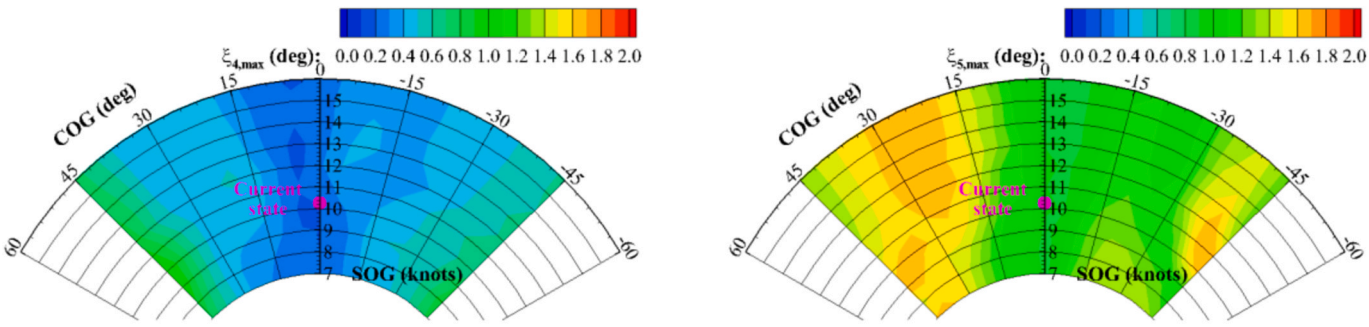

(a) Head sea condition

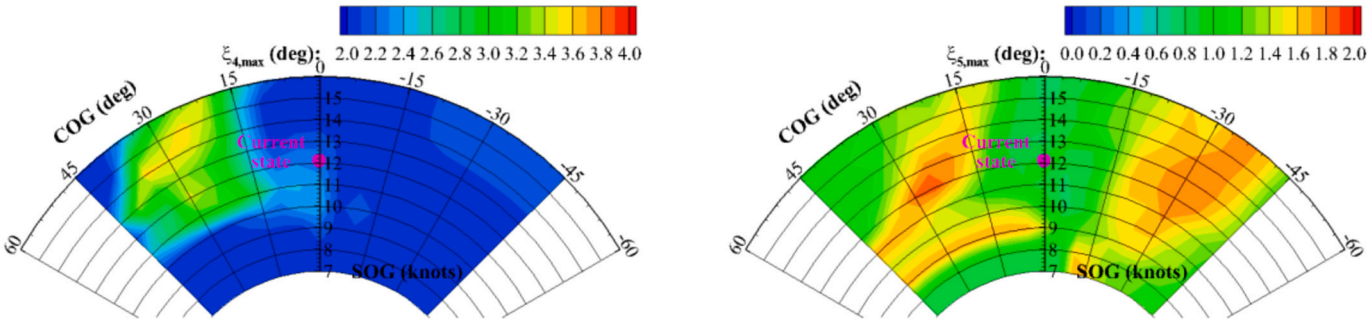

(b) Beam sea condition

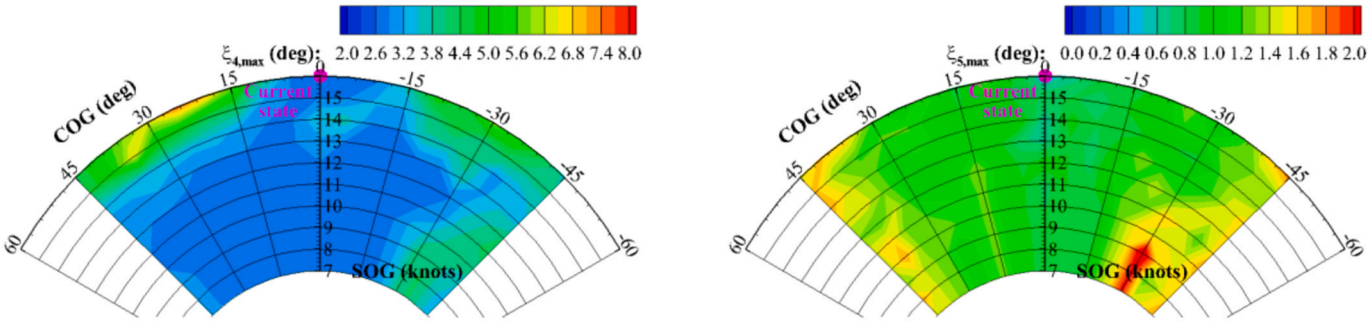

(c) Following sea condition

Fig. 24. Maximum motion responses for various operation scenarios: roll (left) and pitch motions (right), $T = 96\ s$, $R_{\max} = 5.12\ km$

For this prediction, the reference time should be set as close to the end of the sequence as possible, without losing accuracy. In this study, the reference time was set as $t* = t_0 + 3T/4$, according to the correlation of the reconstruction results (see Fig. 14). It should be noted that maneuvering quantities of the free-running simulation were utilized for a predictable time range. Under the head sea, *PI* increased rapidly from the reference time and reached a value close to 1. This indicated that a forecast of almost all the wave components was possible at the ship position. Thereafter, as the waves propagated, *PI* decreased, and the error in the wave prediction increased accordingly. For the reliability of the prediction system, the predictable time ranges ($PI > 0.8$) of two successive sequences should overlap for a certain period. Hence, the duration of a sequence and the time interval between sequences should be adjusted, considering the size and location of the predictable range. Using the free-running simulation record, the ship motions were also predicted beginning from the final instant of measurement. In this simulation, the motion signals obtained using the proposed IRF-based computation and 3D time-domain Rankine panel method coupled with the MMG solver (**Lee and Kim, 2021**) were compared. Based on accurate forecasting with a correlation greater than 0.9 for incident wave trains on the ship (at the radar location), the computed ship motions for each predictable range show good agreements between the two results (the correlation of about 0.8) as shown in Fig. 21. This denotes that the prediction accuracy and the predictable time range for ocean waves can be utilized as a basis for the overall operation of the present system.

In the following sea conditions, the predictable time range was significantly longer as *PI* increased and decreased relatively slowly (Fig. 22). In addition, the predictable range was almost proportional to the maximum sensing radius according to the behaviors of *PI*. However, *PI* did not reach a value close to 1, which meant that some wave components were difficult to forecast. Therefore, the error in wave prediction was more significant than that in head sea conditions. As shown in

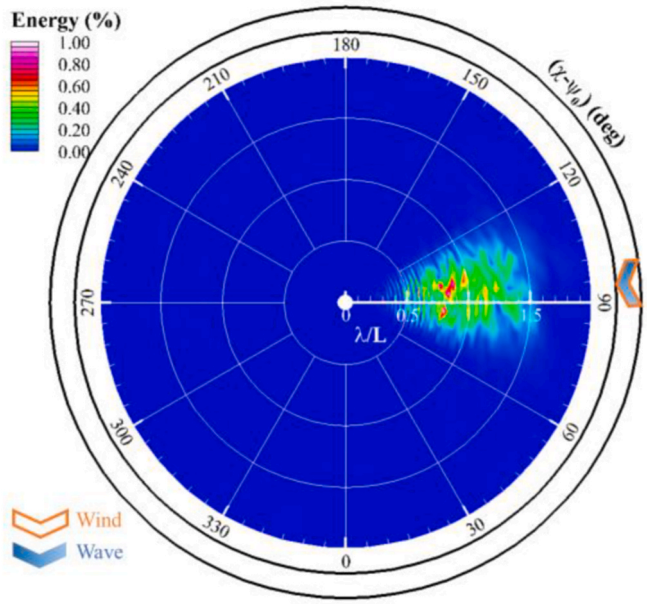

Fig. 25. Wave energy distribution: beam sea condition, $T = 96\ s$, $R_{max} = 5.12\ km$

Fig. 23, some discrepancies were observed between the solutions of the IRF-based and Rankine panel methods. These errors were due to inaccurate waves and the difference between the computational methods for the hydrodynamic forces in the following sea. Furthermore, in the following sea, the starting instant of a predictable range was later than that of the prediction: $t_0 + T < t_s$. Therefore, the wave forecast may not be very accurate between the two instants, but the errors in the ship motion predictions were relatively smaller.

Fig. 24 shows the maximum motion response for each operational scenario. By comparing the prediction values of various scenarios, including the current state, decision support for ship operation is possible. The change in the maximum response was greater according to COG than SOG. Furthermore, the sensitivity of roll motion to COG was significant for the following sea conditions, while the pitch motion varied more for the beam sea condition. Because time-domain computation was required for each scenario, the number of applicable scenarios was determined by the computing power of the prediction system.

3.4. Example of operational guidance

Operational guidance can be established based on the results of the wave and motion analyses. As shown in Fig. 25, through the energy distribution of the phase-resolved wave components in a polar coordinate, the main wavelength and propagation direction could be determined. This wave information was updated in real time for every sequence to detect changes in the ocean environment. As shown in Figs. 26 and 27, the resistance and seakeeping performance were computed for the beam sea conditions. Based on the established operational guidance, the tendency of the environmental loads and ship motions according to the change in the ship speed and yaw angle with respect to the current state were evaluated. This kind of information is helpful for ship operators to make decisions.

4. Conclusions

In this study, a real-time prediction system for wave field and ship operation was developed. To verify the prediction performance of the system, a free-running simulation in real sea states was numerically performed, and synthetic radar images for the corresponding ship operations were utilized. The following conclusions were drawn based on the simulation results:

- To improve the accuracy of wave-field reconstruction, modifications of both the spectral components and image intensity are required to ensure that the radar images have a wave-like intensity distribution.
- The computation parameters for wave-field analysis (duration of a sequence, specifications of radar images, filtering range, etc.) should be optimized to consider the wave energy distribution determined by ship operation. In addition, the system should be operated reflecting the predictable time range and prediction accuracy, which also

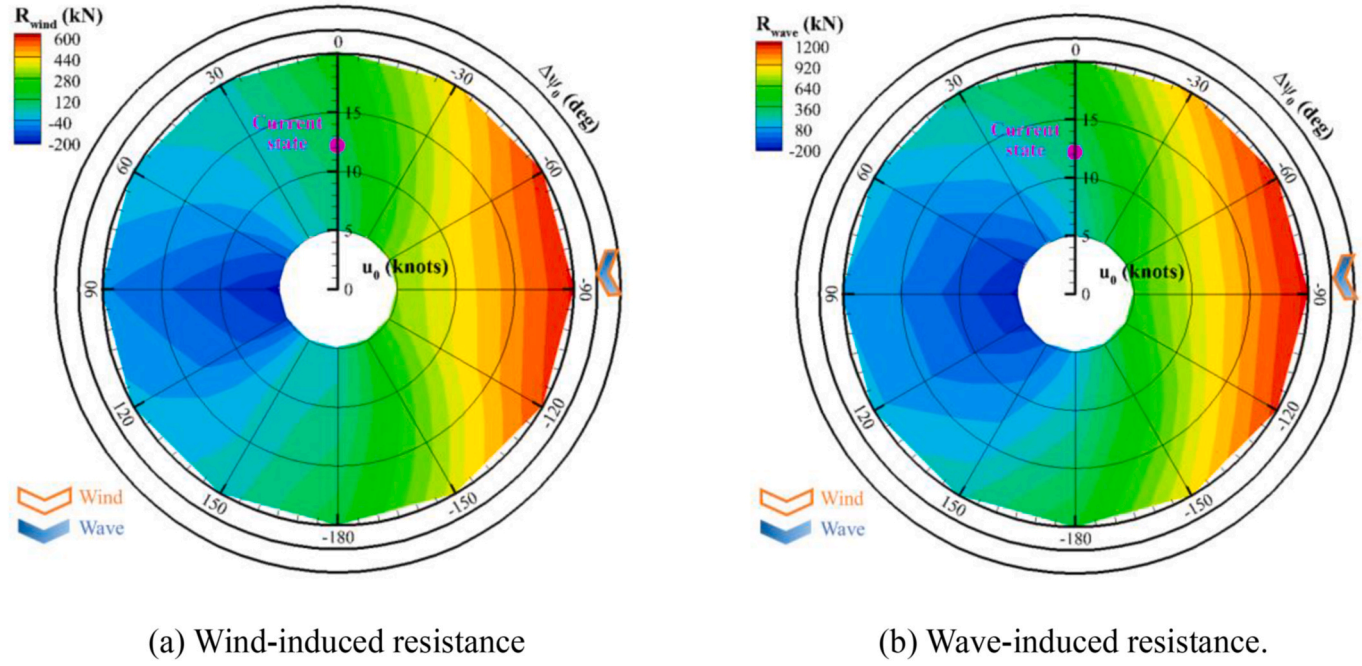

Fig. 26. Resistance performance: beam sea condition, $T = 96\ s$, $R_{max} = 5.12\ km$

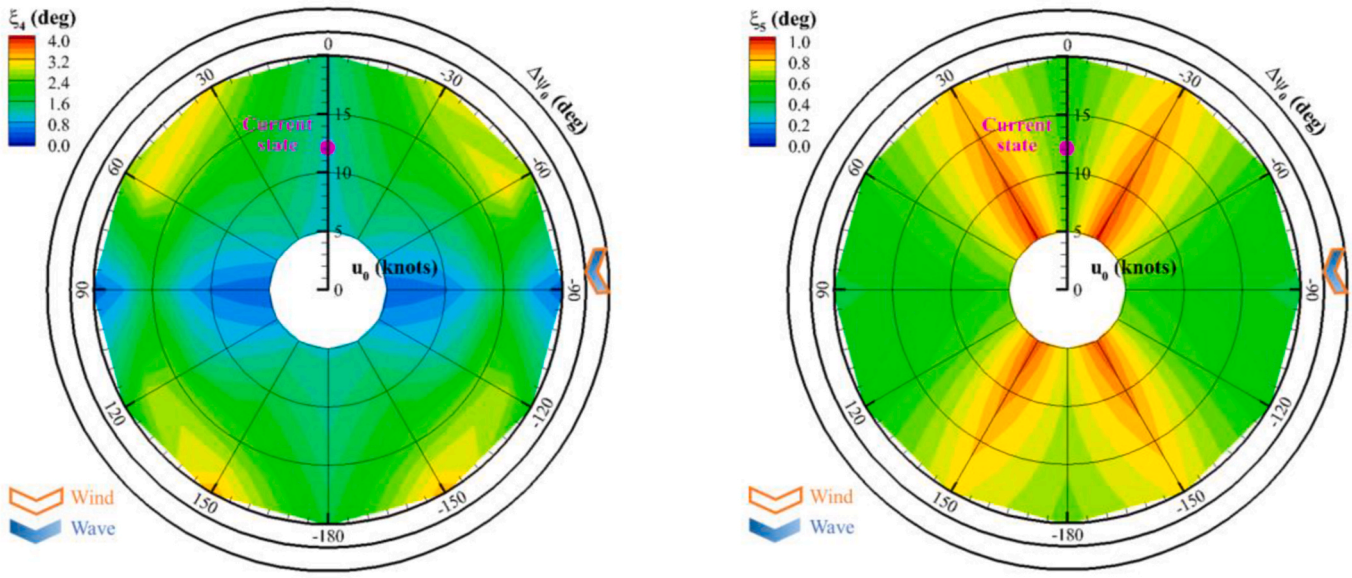

(a) Roll motion (b) Pitch motion

Fig. 27. Significant motions: beam sea condition, $T = 96\ s$, $R_{max} = 5.12\ km$

depends on the relationship between the ship's operational velocity and the main propagation direction of the waves.

- Based on the phase-resolved wave components, operational guidance can be established by comparing the resistance and seakeeping performance for various operation scenarios. In the future, verification of the operational guidance provided by the developed prediction system should be performed based on real radar measurements and a sea trial test.
- This real-time digital twin for ship operation has a significant potential for application and extension. This technique reduces the risk and fuel consumption of ships during waves. Other algorithms related to ship operation and monitoring can be embedded into this system. Eventually, digital schemes based on the collection of actual ship operation data in waves will be combined with this simulation method to improve the prediction accuracy.

CRediT authorship contribution statement

Jae-Hoon Lee: Methodology, Software, Writing – original draft. **Yoon-Seo Nam:** Software, Formal analysis. **Yonghwan Kim:** Conceptualization, Writing – review & editing, Supervision, Project administration. **Yuming Liu:** Supervision. **Jaehak Lee:** Software, Formal analysis. **Heesuk Yang:** Formal analysis.

Declaration of competing interest

The authors declare that they have no known competing financial interests or personal relationships that could have appeared to influence the work reported in this paper.

Data availability

Data will be made available on request.

Acknowledgement

This study was funded by the DSME-SNU Future Ocean Cluster (FOC) center through the project "Development of Core Technology for Real-Time Digital Twin of Ship Operation in Seaways" (No. 0690–2020014). Their support is appreciated. Furthermore, the Research Institute of Marine System Engineering (RIMSE) and the Institute of Engineering Research (IOER) of SNU are credited for their administrative support.

References

Alford, K.K., Beck, R.F., Johnson, J.T., Lyzenga, D., Nwogu, O., Zundel, A., 2014. Design, implementation, and evaluation of a system for environmental and ship motion forecasting. In: Proceedings of the 30th Symposium on Naval Hydrodynamics. Hobart, Tasmania, Australia.

Bekker, A., Suominen, M., Kujala, P., Waal, R.J.O.D., Soal, K.I., 2018. From data to insight for a polar supply and research vessel. Ship Technol. Res. 66 (1), 57–73.

Blondel-Couprie, E., Naaijen, P., 2012. Reconstruction and prediction of short-crested seas based on the application of a 3D-FFT on synthetic waves. Part 2: prediction. In: Proceedings of the 31st International Conference on Ocean, Offshore and Arctic Engineering. Rio de Janeiro, Brazil.

Chen, X., Huang, W., 2021. Spatial-Temporal convolutional gated recurrent unit network for significant wave height estimation from shipborne marine radar data. IEEE Trans. Geosci. Rem. Sens. 60, 1–11.

Clauss, G.F., Kosleck, S., Testa, D., 2012. Critical situations of vessel operations in short-crested seas – forcast decision support system. J. Offshore Mech. Arctic Eng. 134, 031601.

Clauss, G.F., Klein, M., Dudek, M., Onorato, M., 2015. Deterministic non-linear wave forecast and motion prediction for short-term offshore operations. In: Proceedings of the 25th International Ocean and Polar Engineering Conference. Hawaii, USA.

Cummins, W.E., 1962. The impulse response function and ship motions. Schiffstechnik 47 (9), 101–109.

Dannenberg, J., Hessner, K., Naaijen, P., van den Boon, H., Reichert, K., 2010. The on board wave and motion estimator OWME. In: Proceedings of the 20th International Offshore and Polar Engineering Conference. Beijing, China.

Desmars, N., Bonnefoy, F., Grilli, S.T., Ducrozet, G., Perignon, Y., Guerin, C.A., Ferrant, P., 2020. Experimental and numerical assessment of deterministic nonlinear ocean wave prediction algorithms using non-uniformly sampled wave gauges. Ocean. Eng. 212, 107659.

DSME, 2021. Our Innovation Is Achieved through an Undaunted Spirit and Endless Trials. Daewoo Shipbuilding and Marine Engineering (DSME). DSME Report.

Erikstad, S.O., 2019. Designing ship digital services. In: Proceedings of the 18th Conference on Computer and IT Applications in the Maritime Industries, Tullamore, Ireland.

Fonseca, I.A., Gaspar, H.M., 2020. Fundamentals of digital twins applied to a plastic boy boat and a ship scale model. In: Proceedings of the 34th International ECMS Conference on Modelling and Simulation. Wildau, Germany.

Fonseca, I.A., Gaspar, H.M., 2021. Challenges when creating a cohesive digital twin ship: a data modelling perspective. Ship Technol. Res. 68 (2), 70–83.

Fujimoto, W., Waseda, T., 2020. Ensemble-based variational method for nonlinear inversion of surface gravity waves. J. Atmos. Ocean. Technol. 37 (1), 17–31.

Gangeskar, R., 2014. An algorithm for estimation of wave height from shadowing in X-band radar sea surface images. IEEE Trans. Geosci. Rem. Sens. 52 (6), 3373–3381.

Giering, J.E., Dyck, A., 2021. Maritime Digital Twin architecture: a concept for holistic Digital Twin application for shipbuilding and shipping. AT-ATUOM. 69 (12), 1081–1095.
Grieves, M., 2014. Digital Twin: Manufacturing Excellence through Virtual Factory Replication. White Paper. Florida Institute of Technology, Melbourne, FL, USA.
Hessner, K., Reichert, K., Dittmer, J., Nieto-Borge, J.C., Gunther, H., 2001. Evaluation of WAMOS II wave data. In: Proceedings of the 4th International Symposium on Ocean Wave Measurement and Analysis. San Francisco, California, USA.
Hilmer, T., Thornhill, E., 2015. Observations of predictive skill for real-time deterministic sea waves from WAMOS II. In: Proceedings of OCEANS 2015. MTS/IEEE Washington, Washington, DC, USA.
Huang, W., Gill, E., 2012. Surface current measurement under low sea state using dual polarized X-band nautical radar. IEEE J. Sel. Top. Appl. Earth Obs. Rem. Sens. 5 (6), 1868–1873.
ISO, 2015. Ship and Marine Technology – Guidelines for the Assessment of Speed and Power Performance by Analysis of Speed Trial Data. International Organization Standardization (ISO), 15016.
Kollisch, N., Behrendt, J., Klein, M., Hoffmann, N., 2018. Nonlinear real time prediction of ocean surface waves. Ocean. Eng. 157, 387–400.
Kusters, J.G., Cockrell, K.L., Connell, B.S.H., Rudzinsky, J.P., Vinciullo, V.J., 2016. FuterWaves™: a real-time ship motion forecasting system employing advanced wave-sensing radar. In: Proceedings of OCEANS 2016 MTS/IEEE Monterey. California, USA.
Lee, J.H., Kim, Y., 2020. Study on steady flow approximation in turning simulation of ship in waves. Ocean. Eng. 195, 106645.
Lee, J.H., Kim, Y., 2021. Study on ship operation performance in actual seaways using time-domain free-running simulation. Proc. Inst. Mech. Eng. Part M J. Eng. Marit. Environ. 235 (4), 885–904.
Lee, J., Nam, B.W., Lee, J.H., Kim, Y., 2021. Development of enhanced two-time scale model for simulation of ship maneuvering in ocean waves. J. Mar. Sci. Eng. 9 (7), 700.
Lee, J.H., Nam, Y.S., Lee, J., Yang, H., Kim, Y., Liu, Y., 2022. Real-time prediction of ocean wave fields and ship operation. In: Proceedings of the 34th Symposium on Naval Hydrodynamics. Washington, DC, USA.
Naaijen, P., Blondel-Couprie, E., 2012. Reconstruction and prediction of short-crested seas based on the application of a 3D-FFT on synthetic waves. Part 1: reconstruction. In: Proceedings of the 31st International Conference on Ocean, Offshore and Arctic Engineering. Rio de Janeiro, Brazil.
Naaijen, P., Trulsen, K., Blondel-Couprie, E., 2014. Limits to the extent of the spatio-temporal domain for deterministic wave prediction. Int. Shipbuild. Prog. 61, 203–223.
Naaijen, P., Roozen, D.K., Huijsmans, R.H.M., 2016. Reducing operational risks by on-board phase resolved prediction of wave induced ship motions. In: Proceedings of the 35th International Conference on Ocean, Offshore, and Artic Engineering. Busan, Republic of Korea.
Naaijen, P., van Oosten, K., Roozen, K., van't Veer, R., 2018. Validation of a deterministic wave and ship motion prediction system. In: Proceedings of the 37th International Conference on Ocean, Offshore, and Artic Engineering. Madrid, Spain.
Nieto-Borge, J.C., Reichert, K., Dittmer, J., 1999a. Use of nautical radar as a wave monitoring instrument. Coast. Eng. 37, 331–342.
Nieto-Borge, J.C., Hessner, K., Reichert, K., 1999b. Estimation of the significant wave height with X-band nautical radars. In: Proceedings of the 18th International Conference on Ocean, Offshore and Arctic Engineering. St. Johns, Newfoundland. Canada.
Nieto-Borge, J.C., Rodriguez, G.R., Hessner, K., Gonzalez, P.I., 2004. Inversion of marine radar images for surface wave analysis. J. Atmos. Ocean. Technol. 21 (8), 1291–1300.
Pipchenko, O.D., Zhukov, D.S., 2010. Ship control optimization in heavy weather conditions. In: Proceedings of the International Association of Maritime Universities AGA11, Busan, Korea.
Qi, Y., Xiao, W., Yue, D.K.P., 2016. Phase-resolved wave field simulation calibration of sea surface reconstruction using noncoherent marine radar. J. Atmos. Ocean. Technol. 33 (6), 1135–1149.
Qi, Y., Wu, G., Liu, Y., Yue, D.K.P., 2018. Predictable zone for phase-resolved reconstruction and forecast of irregular waves. Wave Motion 77, 195–213.
Salcedo-Sanz, S., Nieto-Borge, J.C., Carro-Calvo, L., Cuadra, L., Hessner, K., Alexandre, E., 2015. Significant wave height estimation using SVR algorithms and shadowing information from simulated real measured X-band radar images of the sea surface. Ocean. Eng. 101, 244–253.
Salvesen, N., Tuck, E.O., Faltinsen, O., 1970. Ship motions and sea loads. Trans. - Soc. Nav. Archit. Mar. Eng. 78, 250–279.
Senet, C.M., Seemann, J., Ziemer, F., 2001. The near-surface current velocity determined from image sequences of the sea surface. IEEE Trans. Geosci. Rem. Sens. 39 (3), 492–505.
Serafino, F., Lugni, C., Soldovieri, F., 2010. A novel strategy for the surface current determination from marine X-band radar data. IEEE Trans. Geosci. Rem. Sens. 7 (2), 231–235.
Simanesew, A., Trulsen, K., Krogstad, H., Nieto-Borge, J.C., 2017. Surface wave predictions in weakly nonlinear directional seas. Appl. Ocean Res. 65, 79–89.
SIMMAN, 2008. Part B: benchmark test cases. In: Proceedings of the Workshop on Verification and Validation of Ship Manoeuvring Simulation Methods, 1. SIMMAN, pp. B3–B14, 2008.
Smogeli, O., 2017. Digital twins at work in maritime and energy. DNV-GL Feature 1 (7).
Stevens, S.C., Parsons, M.G., 2002. Effects of motion at sea on crew performance: a survey. Mar. Technol. SNAME N. 39 (1), 29–47.
Stole-Hentschel, S., Seemann, J., Nieto-Borge, J.C., Trulsen, K., 2018. Consistency between sea-surface reconstructions from nautical X-band radar Doppler and amplitude measurements. J. Atmos. Ocean. Technol. 35 (6), 1201–1220.
Wijaya, A.P., Naaijen, P., Andonowati, E., van Groesen, E., 2015. Reconstruction and future prediction of the sea surface from radar observations. Ocean. Eng. 106, 261–270.
Wijaya, A.P., van Groesen, E., 2016. Determination of the significant wave height from shadowing in synthetic radar images. Ocean. Eng. 114, 204–215.
Wu, G., 2004. Direct Simulation and Deterministic Prediction of Large-Scale Nonlinear Ocean Wave Field. Ph.D. Thesis. MIT, Cambridge, MA, USA.
Yasukawa, H., Yoshimura, Y., 2015. Introduction of MMG standard method for ship maneuvering predictions. J. Mar. Sci. Technol. 20, 37–52.
Yasukawa, H., Hirata, N., Yonemasu, I., 2015. Maneuvering simulation of a KVLCC2 tanker in irregular waves. In: Proceedings of the International Conference on Marine Simulation Ship Manoeuvrability. Newcastle, UK.
Young, I.R., Rosenthal, W., 1985. Three-dimensional analysis of marine radar images for the determination of ocean wave directionality and surface currents. J. Geophys. Res. 90, 1049–1059.
Zinchenko, V., Vasilyev, L., Halstensen, S.O., Liu, Y., 2021a. An improved algorithm for phase-resolved sea surface reconstruction from X-band marine radar images. J. Ocean. Eng. Mar. Energy. 7, 97–114.
Zinchenko, V., Vasilyev, L., Halstensen, S.O., Liu, Y., 2021b. Short-time deterministic prediction of individual waves based on space-time X-band marine radar measurements. Proc. Inst. Mech. Eng. Part M J. Eng. Marit. Environ. 235 (2), 356–371.